

# The (in)stability of quasinormal modes of Boulware-Deser-Wheeler black hole in the hyperboloidal framework

Li-Ming Cao<sup>a, b\*</sup>, Liang-Bi Wu<sup>c, d†</sup>, and Yu-Sen Zhou<sup>a‡</sup>

<sup>a</sup>*Interdisciplinary Center for Theoretical Study and Department of Modern Physics, University of Science and Technology of China, Hefei, Anhui 230026, China*

<sup>b</sup>*Peng Huanwu Center for Fundamental Theory, Hefei, Anhui 230026, China*

<sup>c</sup>*School of Fundamental Physics and Mathematical Sciences, Hangzhou Institute for Advanced Study, UCAS, Hangzhou 310024, China and*

<sup>d</sup>*University of Chinese Academy of Sciences, Beijing 100049, China*

(Dated: December 31, 2024)

We study the quasinormal modes of Boulware-Deser-Wheeler black hole in Einstein-Gauss-Bonnet gravity theory within the hyperboloidal framework. The effective potentials for the test Klein-Gordon field and gravitational perturbations of scalar, vector, and tensor type are thoroughly investigated and put into thirteen typical classes. The effective potentials for the gravitational perturbations have more diverse behaviors than those in general relativity, such as double peaks, the existence of the negative region adjacent to or far away from the event horizon, etc. These lead to the existence of unstable modes ( $\text{Im}\omega < 0$ ), and the presence of gravitational wave echoes. These rich phenomena are inherent in Einstein-Gauss-Bonnet theory, rather than artificially introduced by hand. What's more, the (in)stability of quasinormal modes are studied in frequency domain and time domain, respectively. For the frequency aspect, the pseudospectrum is used to account for the instability of the spectrum. For the time domain, we add a small bump to the effective potential, and find that the new waveform does not differ significantly from the original one, where the comparison is characterized by the so-called mismatch functions. This means that quasinormal modes are stable in time domain. In this way, our study reveals the non-equivalence of the stability of quasinormal modes in the frequency domain and the time domain. We also numerically investigate Price's law at both finite distances and infinity with the assistance of the hyperboloidal approach.

## I. INTRODUCTION

Black holes in higher dimensions have gain more and more attentions in high-energy physics, particularly with the advance of string theory, brane-world scenario, and the theoretical possibility of black hole production at the Large Hadron Collider (LHC) [1–9]. While general relativity (GR) provides a very successful framework for describing gravity, investigations into higher-dimensional black holes often need extensions of GR to address challenges and incorporate new physics [10, 11]. Einstein-Gauss-Bonnet (EGB) gravity theory, which is a natural generalization of GR suggested by Lovelock's theorem [12, 13], emerge as a candidate. EGB gravity theory incorporates a higher-order curvature term, i.e., the Gauss-Bonnet term, into the Einstein-Hilbert action. This term arises naturally in the low-energy effective action of string theory [14–16]. This provides a well-motivated framework for exploring gravitational phenomena in extreme astrophysical and cosmological environments, such as black holes and the early universe. Among the solutions in EGB theory, the Boulware-Deser-Wheeler (BDW) black hole [16, 17] stands out as a static, spherically symmetric solution in higher-dimensional spacetimes and generalizes the Schwarzschild solution of GR to include Gauss-Bonnet corrections. This solution and its generalization incorporated cosmological constant [18] have been extensively studied in the context of gravitational waves, black hole thermodynamics, and holographic property of gravity [19–24].

A crucial aspect of black hole is their stability under perturbations [25]. Linear perturbation theory provides a natural approach to investigate stability, leading to the concept of quasinormal modes (QNMs) [26–29]. QNMs are the solutions to the linear perturbation equations subject to the outgoing boundary conditions. The evolution of a perturbed black hole exhibits distinct stages [30]: an initial prompt response, followed by a damped oscillatory phase described by the superimpositions of QNMs, and finally, a late-time tail decay [31, 32]. The real part of the QNM represents the oscillation frequency, while the imaginary part determines the damping rate, directly relating to stability. In this paper, with our notions, a mode with a negative imaginary part corresponds to an unstable mode. Moreover, QNMs serve as unique fingerprints for black hole identification and characterization in gravitational wave astronomy [28, 33–37].

Solving for QNMs is faced with the boundary conditions and the divergence of eigenfunctions at the boundaries of outer community of the black holes. The hyperboloidal framework [38] offers a powerful approach to overcome these difficulties. By employing constant- $\tau$  slices that extend to null infinity and penetrate the event horizon, the hyperboloidal framework avoids the divergences of eigenfunctions. Furthermore, at boundaries, light-cones point outwards the computational domain, the boundary

\* e-mail address: caolm@ustc.edu.cn

† e-mail address: liangbi@mail.ustc.edu.cn

‡ e-mail address: zhou\_ys@mail.ustc.edu.cn (corresponding author)

conditions are naturally satisfied [39–42]. Compactification of spatial coordinates allows numerical computation to reach the infinity, transforming the QNM problem into a simpler eigenvalue problem in the hyperboloidal framework.

The stability of QNMs is a critical aspect of black hole physics, especially considering the complicated astrophysical environments surrounding black holes [43]. The pioneering work of Nollert and Price shown that even small perturbation can significantly influence the higher overtone modes in the QNM spectra [44, 45]. This phenomenon is known as the spectrum instability, which requires a thorough investigation of the robustness of QNMs against perturbations of the background spacetime. The spectrum instability of QNMs also presents a substantial challenge for their numerical computation, especially for high overtones. For instance, approximations of the effective potential can lead to significant deviations in the QNM spectrum [46, 47].

The spectrum instability can be characterized by pseudospectrum, which is a tool originally developed to analyze non-self-adjoint operators [48, 49]. The dynamics of black hole systems are described by non-self-adjoint operators since they are inherently dissipative. With the help of the hyperboloidal formalism and the pseudo-spectral method, the QNMs problem is recast as an eigenvalue problem. Therefore, the concept of the pseudospectrum provides a powerful framework for studying the stability of QNMs. The  $\epsilon$ -pseudospectrum visually represents an upper bound on the displacement of QNMs under perturbations of norm  $\epsilon$ . The pseudospectrum have gained a lot of attentions in asymptotic flat spacetime [50–52], spacetime with a positive [53–56] or negative [57–61] cosmological constant, and horizonless compact objects [62]. Pseudospectrum can be calculated by evaluating the norm of the resolvent in hyperboloidal coordinates, which involves matrix approximations in numerical schemes [50]. However, the convergence of the matrix-derived pseudospectrum to the true operator pseudospectrum in asymptotically flat spacetimes as the grid resolution increases remains an open question. Choose higher-order Sobolev norms may alleviate this problem [59]. Nevertheless, despite potential quantitative discrepancies, pseudospectra provide a valuable qualitative understanding of spectral migration and the sensitivity of QNMs to perturbations.

Simultaneously, the question of time-domain stability has been a focus of considerable research [63, 64]. While frequency-domain analyses often suggest instability, the analysis in the time domain indicates stability. Some studies shown that certain quantities resulting from the scattering properties are unaffected by spectrum instabilities [65–68]. This apparent contradiction needs further study to address these seemingly different results.

Understanding the (in)stability of QNMs is crucial for characterizing black hole perturbations and testing gravity theories. In this work, we investigate the dynamics of perturbations around a BDW black hole, analyzing its effective potentials and calculating QNMs in both the time and frequency domains. We employ two complementary approaches to assess (in)stability: pseudospectrum in the frequency domain and waveform mismatch in the time domain. Furthermore, we validate our numerical code by calculating Price’s law.

This paper is organized as follows. In Sec. II, the hyperboloidal framework of the BDW black hole is introduced. In Sec. III, we get the QNMs from the frequency domain and the time domain, respectively. In Sec. IV, we study the stabilities of QNMs in frequency domain and time domain, respectively. Sec. V is the conclusions and discussion. Criteria for identifying physically relevant QNM spectra in given in Appendix. A.

## II. THE HYPERBOLOIDAL FRAMEWORK OF THE BOULWARE-DESER-WHEELER BLACK HOLE

We begin this section by reviewing the Boulware-Deser-Wheeler (BDW) black hole in the Einstein-Gauss-Bonnet gravity theory. The action of the EGB gravity theory is

$$S = \frac{1}{16\pi G_D} \int d^D x \sqrt{-g} (R + \tilde{\alpha} L_{\text{GB}}), \quad D \geq 5, \quad (2.1)$$

where the Gauss-Bonnet term  $L_{\text{GB}}$  is given by

$$L_{\text{GB}} = R_{abcd}R^{abcd} - 4R_{ab}R^{ab} + R^2, \quad (2.2)$$

$\tilde{\alpha}$  is a positive coupling constant and  $G_D$  is the  $D$ -dimensional Newtonian constant of gravitation. The static vacuum solutions in EGB gravity were found long time ago by Boulware and Deser [16] and Wheeler [17]. The metric of the solution can be expressed as

$$ds^2 = -f(r)dt^2 + f(r)^{-1}dr^2 + r^2 d\Omega_{D-2}^2, \quad (2.3)$$

where the metric function is

$$f(r) = 1 + \frac{r^2}{2\tilde{\alpha}(D-3)(D-4)} \left( 1 - \sqrt{1 + \frac{8\tilde{\alpha}(D-3)(D-4)\tilde{\mu}}{(D-2)r^{D-1}}} \right), \quad (2.4)$$

$\tilde{\mu}$  is the mass parameter of the back hole, and  $d\Omega_{D-2}^2$  is the line element of a  $(D-2)$ -dimensional unit sphere. This black hole has only one horizon, that is, the event horizon  $r_+$ . Therefore, by using  $f(r_+) = 0$ , the mass parameter  $\tilde{\mu}$  can be expressed in

terms of the black hole horizon event  $r_+$  as follow

$$\tilde{\mu} = \frac{(D-2)r_+^{D-3}}{2} \left[ 1 + \frac{\tilde{\alpha}(D-3)(D-4)}{r_+^2} \right]. \quad (2.5)$$

For simplicity, we introduce two dimensionless quantities,

$$\mu = \frac{\tilde{\mu}}{r_+^{D-3}}, \quad \alpha = \frac{\tilde{\alpha}}{r_+^2}. \quad (2.6)$$

From the definitions (2.6) and Eq.(2.5), two dimensionless quantities have the following relation,

$$\mu = \frac{(D-2)}{2} \left[ 1 + \alpha(D-3)(D-4) \right]. \quad (2.7)$$

The above equation indicates that there is only one independent dimensionless parameter in the BDW black hole. For convenience,  $\alpha$  is chosen as the free dimensionless parameter. One thing that needs to be emphasized is that even though the actual  $\tilde{\alpha}$  may be small,  $\alpha$  can also take a large value regarding a small black hole, i.e.,  $r_+$  is small.

For the BDW black hole we are currently considering, we consider not only a test scalar field, but also the gravitational perturbations. The test scalar field obeys the Klein-Gordon equation, and linear perturbations in EGB gravity can be classified into scalar, vector, and tensor types generally. The equations of gravitational perturbations and the Klein-Gordon equation for the BDW black hole can be all decoupled into radial and angular parts. The radial part reduces to a wave-like equation,

$$\left( \frac{\partial^2}{\partial t^2} - \frac{\partial^2}{\partial r_*^2} + \tilde{V}_X(r) \right) \Psi(t, r) = 0, \quad dr_* = \frac{dr}{f(r)}, \quad (2.8)$$

in which  $X$  refers to  $K, S, V, T$  and they represent the effective potentials of KG equation, scalar perturbation, vector perturbation and tensor perturbation, respectively. The explicit expressions of the effective potentials for these four sectors are very cumbersome and can be found in [69–76]. One should be aware that the potential  $\tilde{V}_X(r)$  depends on the multipole number  $l$ . For the KG equation, the integer  $l$  starts from 0, but for gravitational perturbations, the integer  $l$  starts from 2 [71].

Following [40], for the BDW black hole, we study the compact hyperboloidal coordinates  $(\tau, \sigma, \theta, \phi)$  related with original coordinate  $(t, r, \theta, \phi)$  as follows

$$\begin{aligned} t &= r_+ [\tau - h(\sigma)], \\ r &= \frac{r_+}{\sigma}, \end{aligned} \quad (2.9)$$

where  $h(\sigma)$  is called the height function. The domain of  $\sigma$  is restricted to  $[0, 1]$  where  $\sigma = 0$  and  $\sigma = 1$  corresponds to the null infinity  $\mathcal{I}^+$  and the event horizon  $\mathcal{H}$ , respectively. The method provided by [40] states that there are two common and alternative approaches to derive the explicit expressions of  $h(\sigma)$ : in-out and out-in strategies, which gives out different height functions

$$h'_{\text{in-out}}(\sigma) = \frac{2}{\sigma^2} - \frac{1}{\sigma^2 F(\sigma)}, \quad (2.10)$$

$$h'_{\text{out-in}}(\sigma) = -\frac{1 + 2(D-3)(D-4)\alpha}{(D-3)[1 + (D-4)(D-5)\alpha]} \frac{2}{1-\sigma} + \frac{1}{\sigma^2 F(\sigma)}, \quad (2.11)$$

where

$$F(\sigma) \equiv f(r(\sigma)) = 1 + \frac{1}{2(D-3)(D-4)\alpha\sigma^2} \left( 1 - \sqrt{1 + 4(D-4)(D-3)[1 + (D-4)(D-3)\alpha]\alpha\sigma^{D-1}} \right), \quad (2.12)$$

and prime denotes differentiation with respect to  $\sigma$ . Using the compact hyperboloidal coordinates (2.9), we can recast Eq.(2.8) into a form of a hyperbolic equation,

$$\partial_\tau u = Lu, \quad L = \begin{pmatrix} 0 & 1 \\ L_1 & L_2 \end{pmatrix}, \quad u = \begin{pmatrix} \Psi \\ \Pi \end{pmatrix}, \quad (2.13)$$

where  $\Pi = \partial_\tau \Psi$  is introduced to reduce the time derivative order in the equation. The differential operators  $L_1$  and  $L_2$  in

Eq.(2.13) are written in Sturm-Liouville form,

$$L_1 = \frac{1}{w(\sigma)} \left[ \partial_\sigma (p(\sigma) \partial_\sigma) - q_X(\sigma) \right], \quad (2.14)$$

$$L_2 = \frac{1}{w(\sigma)} \left[ 2\gamma(\sigma) \partial_\sigma + \partial_\sigma \gamma(\sigma) \right], \quad (2.15)$$

where the explicit forms of the above functions are given as follows

$$p(\sigma) = \sigma^2 F(\sigma), \quad \gamma(\sigma) = h'(\sigma) p(\sigma), \quad w(\sigma) = \frac{1 - \gamma(\sigma)^2}{p(\sigma)}, \quad q_X(\sigma) = \frac{1}{p(\sigma)} V_X(\sigma), \quad (2.16)$$

and  $V_X(\sigma) = r_+^2 \tilde{V}_X(\sigma)$  is the dimensionless effective potential with  $\tilde{V}_X(\sigma) = \tilde{V}_X(r(\sigma))$ . Moreover, it can be found that  $w(0) = 0$  for  $D > 5$  within the in-out strategy, indicating that the hypersurfaces  $\tau = \text{constant}$  will become asymptotically null. Therefore, we adopt solely the out-in strategy and omit the subscript. So far, we have established the hyperboloidal framework of the BDW black hole. Here, such hyperboloidal framework refers to the PDE system [Eq.(2.13)-Eq.(2.16)], in which  $L$  is the infinitesimal generator of time evolution.

Since the shape of the effective potential can significantly influence the time-domain behavior and QNM spectra, in Fig.1, we show several typical effective potentials, which will be served as benchmarks for subsequent studies. Four panels of Fig.1 represent the effective potentials  $V_X(\sigma)$ , with the coordinate  $\sigma$  as the variable, for KG type, scalar type, vector type, tensor type perturbations in turn. From the first panel, the KG case presents a straightforward single-peaked positive potential barrier. In contrast, the scalar, vector, and tensor perturbation cases display more intricate behaviors. These potentials can feature double-peaked structures, with or without negative regions that may arise either adjacent to or separate from the event horizon. It is worth mentioning that although the second and third parameters of both the scalar and tensor perturbations share similar characteristics (see the yellow and green lines of the second panels and the fourth panels of Fig.1), exhibiting a single peak and a negative region adjacent to the horizon, their QNM spectra and time-domain behaviors differ unexpectedly. The second parameters (yellow lines) are stable, showing no unstable QNMs and remaining well-behaved over time, but instability arises in the third parameters (green lines) when the potential's negative region exceeds a critical depth. Therefore, we treat them as two distinct cases. These structures emerge naturally from EGB theory under varying parameters rather than artificially imposed ones. These cases are quite different from the situation under the framework of general relativity where the effective potential exhibits only a single peak. The presence of double-peaked structures and negative regions renders some traditional methods like WKB approximation invalid to get the QNM frequencies, while at the same time the irrational nature of the metric function  $f(r)$  makes the continued fraction method inapplicable [28]. A significant advantage of the pseudo-spectral method is its ability to circumvent these difficulties and its high versatility.

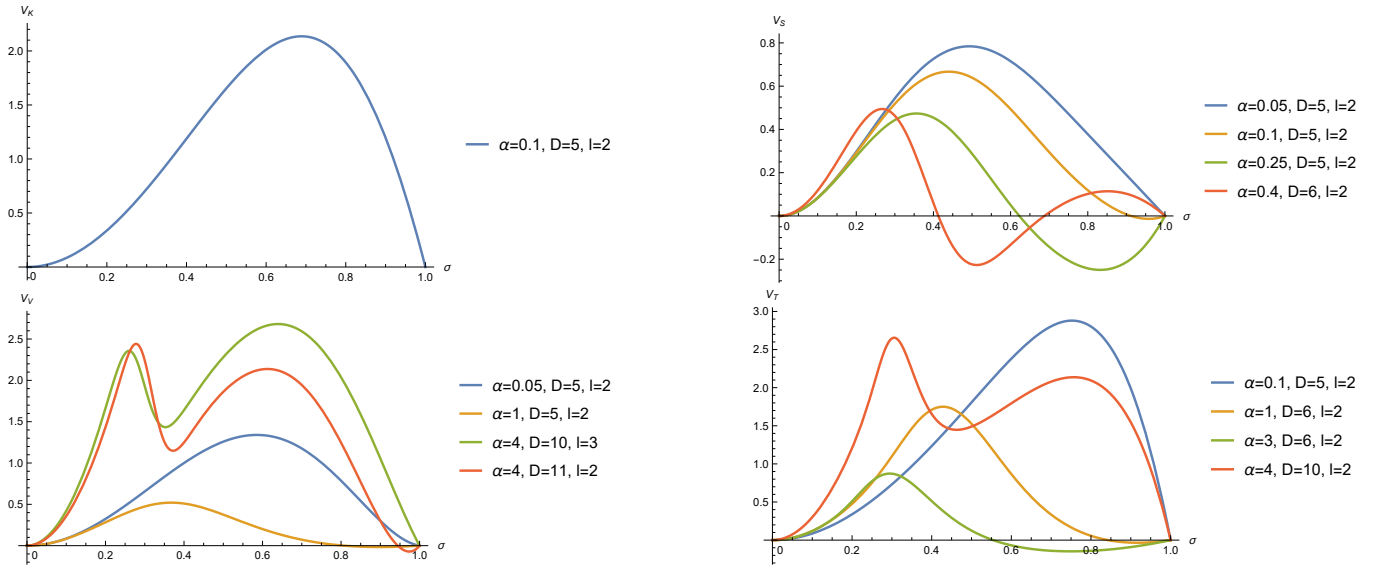


Figure 1: Some typical behaviors of effective potentials  $V_X(\sigma)$  in terms of the coordinate  $\sigma$ . With the exception of the KG case, four typical effective potentials are shown for all three other cases. The top row shows the potentials for the KG equation and scalar perturbation, while the bottom row depicts the potentials for vector and tensor perturbations.  $\sigma = 0$  and  $\sigma = 1$  corresponds to null infinity  $\mathcal{I}^+$  and event horizon  $\mathcal{H}$  respectively.

### III. THE QUASINORMAL MODES

In this section, we start from Eq.(2.13)-Eq.(2.16) to analyze the QNMs of the BDW black hole by computing spectra in the frequency domain and simulating the time-domain behavior. As a basis, we first introduce the pseudo-spectral method used. We discretize the spatial domain on a grid  $\{\sigma_i\}_{i=0}^N$ , converting the original PDE system to a coupled ODE system. The state vector  $u(\tau, \sigma)$  is evaluated in such a spatial grid so that  $\Psi(\tau, \sigma)$  is converted to  $\Psi_i(\tau) \equiv \Psi(\tau, \sigma_i)$ , and  $\Pi(\tau, \sigma)$  is converted into  $\Pi_i(\tau) \equiv \Pi(\tau, \sigma_i)$ . Thus, the problem reduces to the solution of ODEs involving the variables  $\Psi_i(\tau)$  and  $\Pi_i(\tau)$  for  $i = 0, \dots, N$ . Finally, Eq.(2.13) amounts to a system of  $(2N + 2)$  ODEs associated with the time variable  $\tau$  via

$$\frac{d}{d\tau} \begin{bmatrix} \Psi_i \\ \Pi_i \end{bmatrix} = \sum_{j=0}^N \begin{bmatrix} 0 & \delta_{ij} \\ C_i(\mathbf{D}^2)_{ij} + E_i \mathbf{D}_{ij} + W_i \delta_{ij} & A_i \mathbf{D}_{ij} + B_i \delta_{ij} \end{bmatrix} \begin{bmatrix} \Psi_j \\ \Pi_j \end{bmatrix}, \quad i = 0, 1, \dots, N-1, N. \quad (3.1)$$

where  $A_i = A(\sigma_i)$ ,  $B_i = B(\sigma_i)$ ,  $C_i = C(\sigma_i)$ ,  $E_i = E(\sigma_i)$ ,  $W_i = W(\sigma_i)$  and  $\delta_{ij}$  is the Kronecker delta. These five functions  $C(\sigma)$ ,  $E(\sigma)$ ,  $W(\sigma)$ ,  $A(\sigma)$  and  $B(\sigma)$  are directly derived from Eq.(2.14) and Eq.(2.15). There is no summation over  $i$  in the above equation (3.1). The specific form of the differential matrix  $\mathbf{D}^1$  is determined by the chosen Chebyshev-Lobatto grid, given by

$$\sigma_j = \frac{1}{2} \left( 1 + \cos \left( \frac{j\pi}{N} \right) \right), \quad j = 0, 1, \dots, N-1, N. \quad (3.2)$$

The expression of the differential matrix  $\mathbf{D}$  associated with the Chebyshev-Lobatto grid can be found in [50, 52, 77].

In frequency domain, consider the Fourier transform of  $u(\tau, \sigma)$  with respect to time  $\tau$ , we have

$$u(\tau, \sigma) = e^{i\tilde{\omega}t} \tilde{u}(r_*) = e^{i\omega\tau} u(\sigma), \quad (3.3)$$

where  $\omega = r_+ \tilde{\omega}$  is the nondimensionalized frequency, and  $u(\sigma) = e^{-i\omega h(\sigma)} \tilde{u}(r_*)$ . For Eq.(2.8) within the Schwarzschild-like coordinates, since all the constant- $t$  surfaces intersect the spatial infinity  $i^0$  and the bifurcation sphere  $\mathcal{B}$  simultaneously, the QNM eigenfunction  $\tilde{u}(r_*)$  diverges at both boundaries. Therefore, QNM boundary conditions must be carefully imposed, and it is required that a prior separation of the divergent part of  $\tilde{u}(r_*)$ . In contrast, the hyperboloidal formalism, where the constant- $\tau$  surface ends at null infinity  $\mathcal{I}^+$  and penetrates the future event horizon  $\mathcal{H}^+$ , naturally extracts the divergent part,  $e^{i\omega h(\sigma)}$ , through a coordinate transformation. Moreover, the light-cones point outward at the boundary of the computation domain, simplifying boundary conditions to merely requiring a regular solution  $u(\sigma)$ , which is trivially satisfied in numerical calculations. Accordingly, the hyperboloidal formalism provides a significant advantage for computing QNMs [42].

In the numerical calculations, the operator  $L$  is approximated by a matrix operator  $\mathbf{L}$  by using the Chebyshev-Lobatto grid. Therefore, the problem of solving QNM frequencies now turns into a finite-dimensional algebraic eigenvalue problem

$$\mathbf{L}\mathbf{u} = i\omega\mathbf{u}, \quad (3.4)$$

where the matrix  $\mathbf{L}$  above is exactly the coefficient matrix of the right-hand of Eq.(3.1). Although numerical approaches can yield modes that closely approximate true physical modes, they are always accompanied by undesired numerical spurious modes. This requires us to find a way to distinguish between the two. A reliable method based on defining the drifts among the QNM spectra can be found in [58, 77–79]. One can refer to Appendix.A to get more technical details about such method. The spherical symmetry of spacetime results in the matrix  $\mathbf{L}$  being pure real, which implies that both  $\omega$  and  $-\bar{\omega}$  are eigenvalues of Eq.(3.4), where bar represents the complex conjugate. Consequently, QNM frequencies are symmetric about the imaginary axis in the complex frequency plane. Therefore, we only present modes with a non-negative real part. The branch cut in our asymptotically flat spacetime leads to a continuous spectrum along the positive imaginary axis. So we exclude this region from our definitions of the nearest drift (see Appendix.A).

The above statements concern about the calculation of QNM spectra on the frequency domain. Now we turn to time-domain behavior of QNMs. For the time domain case, we have ODEs (3.1) from Eq.(2.13). To solve the ODEs numerically, we adopt a discrete time evolution scheme via 6-th Hermite integration method [80–83], which is actually an implicit scheme. Selecting an even time step  $\Delta\tau$ , we arrive at

$$\mathbf{u}((i+1)\Delta\tau) = \mathbf{U} \cdot \mathbf{u}(i\Delta\tau), \quad i = 0, 1, \dots, \quad (3.5)$$

<sup>1</sup> We use bold symbols to represent matrices and vectors.

where  $\mathbf{U}$  is called evolution matrix whose explicit form can be expressed as

$$\mathbf{U} = \mathbf{I} + (\Delta\tau\mathbf{L}) \cdot \left( \mathbf{I} + \frac{1}{60}(\Delta\tau\mathbf{L}) \cdot (\Delta\tau\mathbf{L}) \right) \cdot \left( \mathbf{I} - \frac{\Delta\tau}{2}\mathbf{L} \cdot \left( \mathbf{I} - \frac{\Delta\tau}{5} \cdot \left( \mathbf{I} - \frac{\Delta\tau}{12}\mathbf{L} \right) \right) \right)^{-1}, \quad (3.6)$$

and  $\mathbf{I}$  is the identity matrix whose dimension is consistent with that of  $\mathbf{L}$ . Because such scheme is unconditionally stable, there is no Courant limit on the time step  $\Delta\tau$ . Meanwhile, there is no requirement for even time steps, i.e.,  $\Delta\tau$  can depend on  $i$ . For convenience, we simply take even time steps in our practice.

For initial data, we choose a Gaussian pulse on the coordinate  $\sigma$  as the initial perturbation, i.e.,

$$\begin{aligned} \Psi(\tau = 0, \sigma) &= a_0 \exp \left[ -\frac{(\sigma - c_0)^2}{2b_0^2} \right], \\ \Pi(\tau = 0, \sigma) &= 0, \end{aligned} \quad (3.7)$$

where  $a_0$  is the amplitude,  $b_0$  is width and  $c_0$  is the position of the Gaussian pulse.

In the hyperboloidal framework, the compactified coordinates ensure that the black hole horizon and null infinity can be reached, while in the usual Schwarzschild-like coordinates, we cannot strictly discuss the infinity without using extra methods. We show the main results of this section in Fig.2, where the parameters used are from Fig.1, and the time evolution is seen by an observer located at infinity ( $\sigma_0 = 0$ ). The computation is done on a grid of resolution  $N = 150$  for QNM spectra, and on a grid of resolution  $N = 160$  with time step  $\Delta\tau = 0.075$ . The initial condition for time domain is chosen as Eqs.(3.7) with  $a_0 = 1$ ,  $b_0 = 1/(10\sqrt{10})$ , and  $c_0 = 1/5$ . Note that Fig.2 has a total of 26 subfigures (a)-(z). The odd sequences [like (a), (c),  $\dots$ , (y)] show the QNM spectra and the even sequences [like (b), (d),  $\dots$ , (z)] show the corresponding time-domain waveforms. These time-domain figures show the logarithm of the absolute value of the waveform. The phase dominated by a single QNM in the time-domain figure exhibits a series of interconnected bell-like shapes. Such shape reflects the characteristics of the QNM. A wider bell opening corresponds to a smaller real part of the QNM spectrum, and a steeper slope of the envelope at the bell's peak indicates a larger imaginary part of the QNM spectrum. The results of these 13 sets of parameters present different characteristics of QNMs, which we summarize as follows.

First, it can be seen that for the parameters leading to double-peaked effective potentials, there exists long-lived modes depicted in Figs.2(i), 2(o), 2(q) and 2(y), and at the same time the echoes will occur in Figs.2(j), 2(p), 2(r), 2(z). Long-lived modes indicate the echo pattern, which decays slowly and persist for a long period, covering up the power-law tail for a long time. Furthermore, the echo pattern also displays a rise phase after the first decay phase, as is shown in Fig.3. Fig.3 presents four panels: the first zooms in on Fig.2(j) (with identical parameters), while the remaining three zoom in on Figs. 2(p), 2(r), and 2(z) (using their parameters but with initial conditions  $b_0 = 1/100$  to highlight the echo pattern). In these four plots, it is evident that the dominant QNM during the first decay phase differs from the one dominating the subsequent rise phase. This transition marks the emergence of the echo mode, which begins to dominate thereafter.

Second, the dynamics instability is previously reported by [71, 75, 76], which is triggered by large  $\alpha$  for scalar type in 5-dimensional spacetime and for tensor type in 6-dimensional spacetime. Similarly, it is also observed that there exists the dynamics instability, i.e., an exponential growth in the time domain simulations in Fig.2(h) and Fig.2(x). The QNM spectra corresponding to these two subfigures are shown in Figs.2(g) and 2(w), and both of them have the mode with a negative imaginary part. Additionally, we find that these unstable modes always appear on the negative half of the imaginary axis. These modes do not migrate from stable modes, but rather, they appear abruptly on the imaginary axis. The slope of the fitting lines precisely match the imaginary part of the corresponding unstable modes.

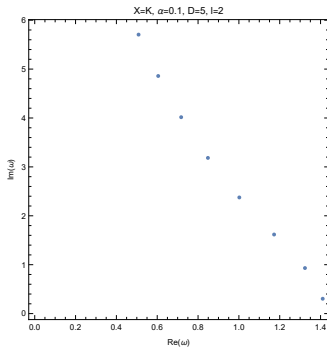
We end this section with an analysis of the Price's law [31, 32]. The analysis of the Price's law can further verify the reliability of our code. The analytical method of [84, 85] shows that the Price's law obtained by a finite-distant observer is determined by the asymptotic behavior of effective potential near infinity. Although the forms of the effective potentials for different perturbations vary, these effective potentials exhibit similar asymptotic behavior at infinity, i.e.,

$$\frac{V_X}{r_+^2} = \frac{\nu(\nu + 1)}{r_*^2} + \frac{A_X}{r_*^{D-1}} + o\left(\frac{1}{r_*^{D-1}}\right), \quad (3.8)$$

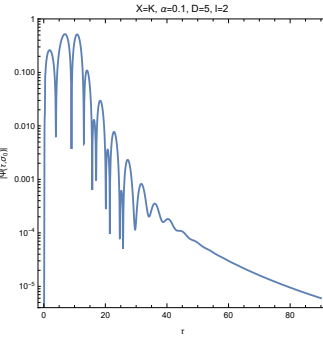
where

$$\nu = \frac{1}{2}(D - 4 + 2l), \quad (3.9)$$

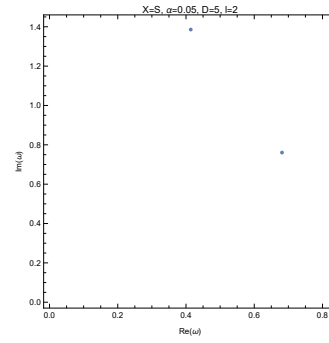
$dr_* = dr/f(r)$  is the tortoise coordinate,  $A_X$  depends on  $\alpha$ ,  $D$ ,  $l$  and does not vanish except when  $X = K$  and  $l = 0$ . In this case, the next leading term is given by  $r_*^{-(2D-4)}$ . Therefore, from [84, 85], the Price's law should be  $D - 2 + 2l$  for observers at finite position in odd dimensions of spacetime. Following [86, 87], we introduce an effective power-law index  $\Gamma$  for



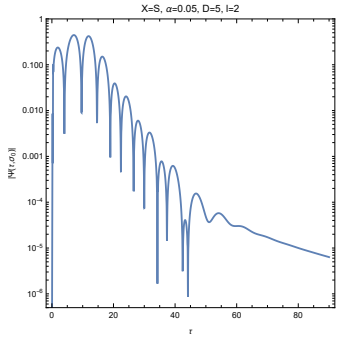
(a)



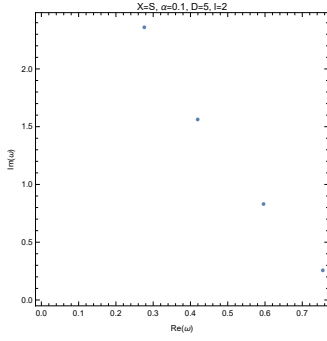
(b)



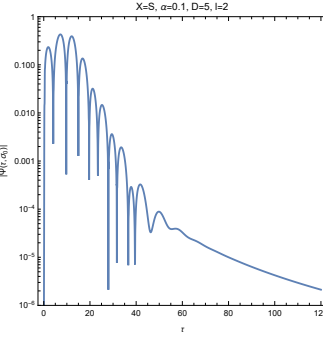
(c)



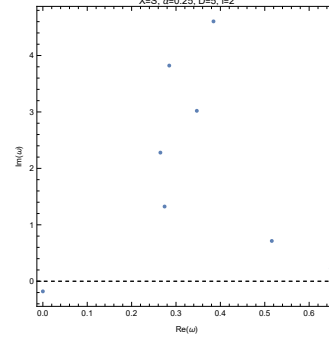
(d)



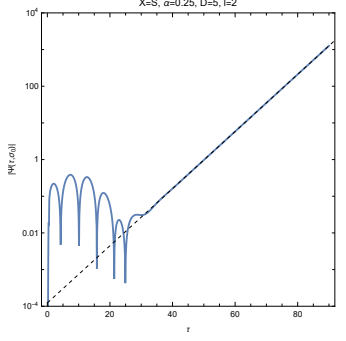
(e)



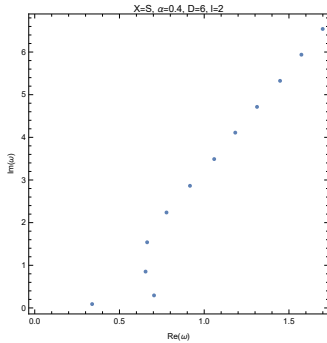
(f)



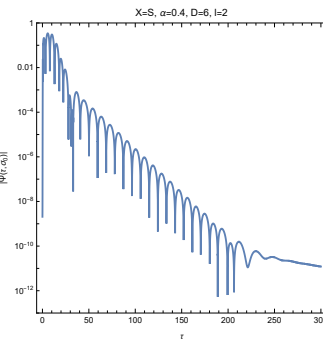
(g)



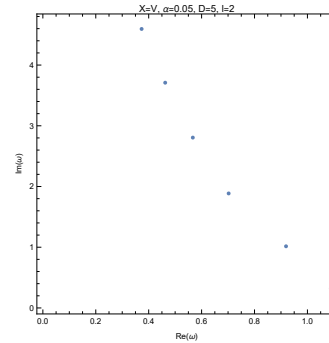
(h)



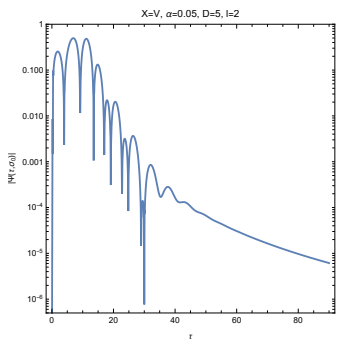
(i)



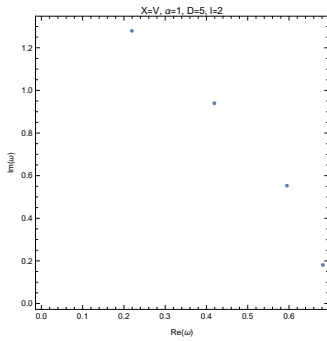
(j)



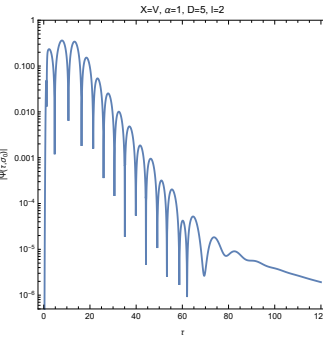
(k)



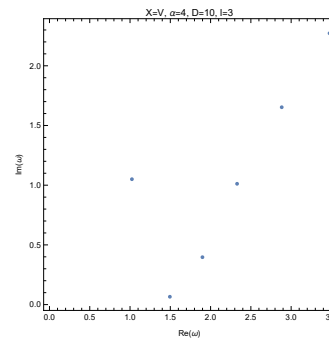
(l)



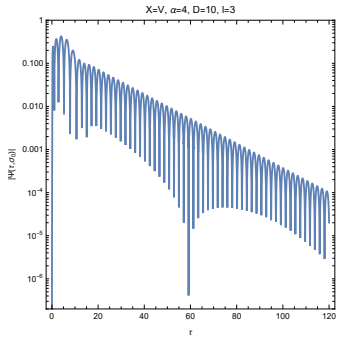
(m)



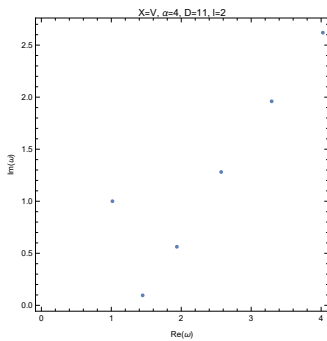
(n)



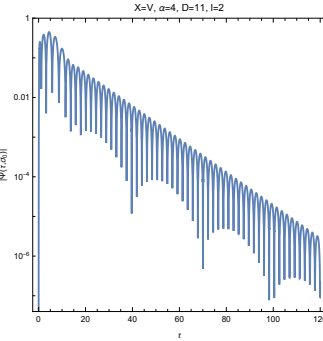
(o)



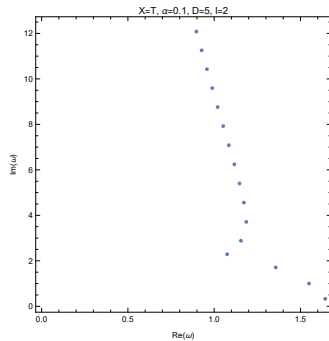
(p)



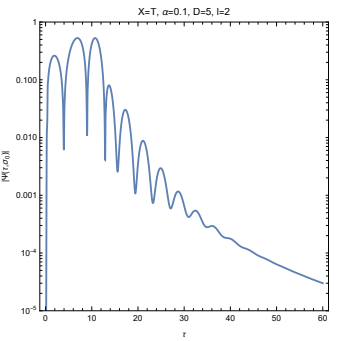
(q)



(r)



(s)



(t)

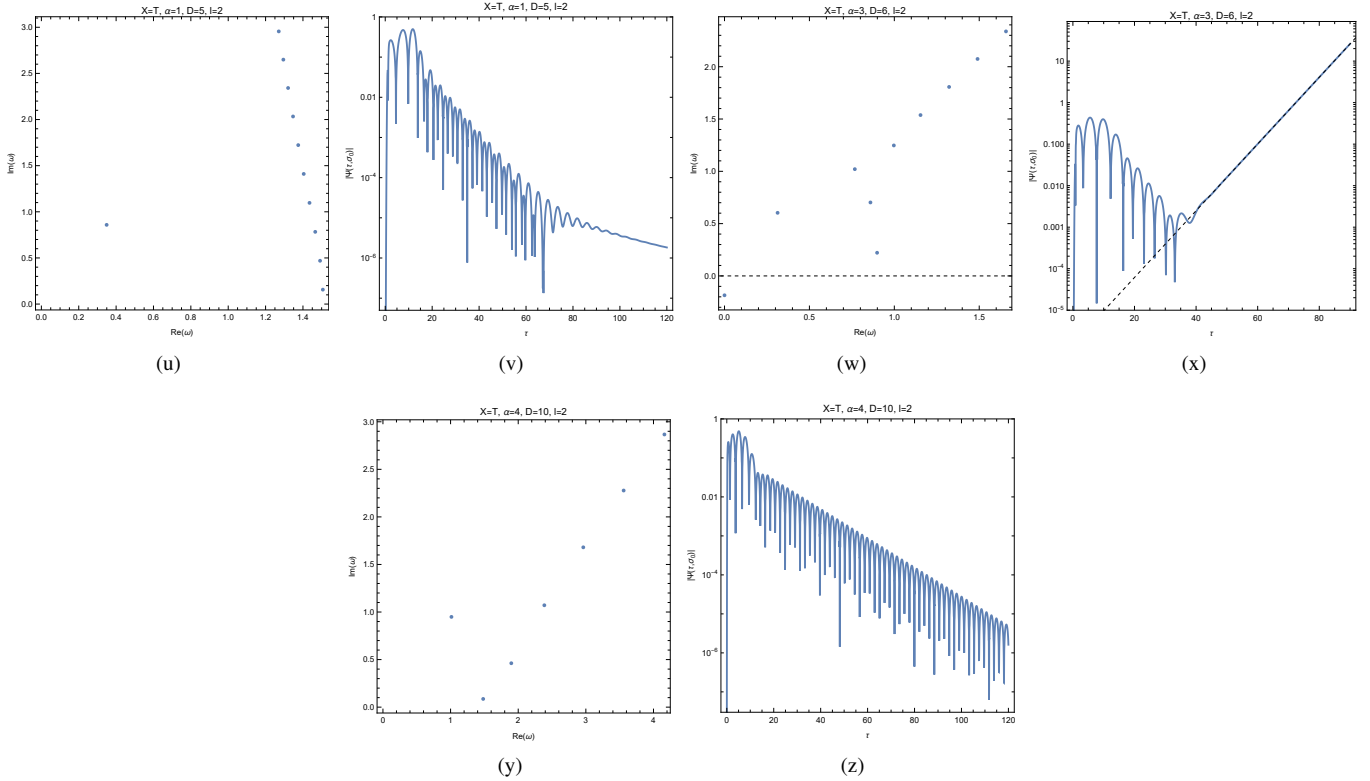


Figure 2: The QNM spectra and time-domain evolution for the parameter choices in Fig.1. The initial condition in time domain calculation is chosen as  $a_0 = 1$ ,  $b_0 = 1/(10\sqrt{10})$  and  $c_0 = 1/5$ . The calculation of QNMs is performed on the resolution with  $N = 150$ , the time domain evolution is performed on a grid with  $N = 160$  using time step  $\Delta\tau = 0.075$ , and the observer is located at infinity, i.e.,  $\sigma_0 = 0$ .

an observer located at  $\sigma_0$ :

$$\Gamma(\tau, \sigma_0) = \left| \frac{\tau \Pi(\tau, \sigma_0)}{\Psi(\tau, \sigma_0)} \right|, \quad (3.10)$$

which should tend to the true Price's law index at late times, i.e.,  $\tau \rightarrow \infty$ . Fig.4 presents the computed effective power-law index  $\Gamma$ . The initial condition is chosen to be Eqs.(3.7) with  $a_0 = 1$ ,  $b_0 = 1/(10\sqrt{10})$ , and  $c_0 = 1/5$ . The observation position  $\sigma_0$  is approximately 0.118 for the left column and is 0 for the right column. The computation is performed on a grid with resolution  $N = 300$  and the time step  $\Delta\tau = 0.075$ . After an initial period of strong oscillation, the index  $\Gamma$  stabilizes to a constant, indicating the presence of a power-law tail and marking the transition from the damping stage to the power-law tail stage. For finite-distant observer,  $\Gamma$  converges to 1, 3, 5, and 7 for  $l = 0, 1, 2$ , and 3, respectively, in the case of KG perturbations. Similarly, it converges to 5, 7, 9, and 11 for  $l = 2, 3, 4$ , and 5, respectively, in the case of gravitational perturbations. For observers located at infinity, the index  $\Gamma$  stabilizes at approximately half of the corresponding values observed by the finite observer. Rigorous proofs using analytical method need to be considered further, and we leave it for the future. These numerical results for finite-distance observers show excellent convergence and agree with the analytical prediction  $D - 2 + 2l$  in odd dimension, which does not depend on  $\alpha$  and is the same as in GR. This behavior is a feature of odd-dimensional spacetimes and does not depend on the presence of a black hole [70, 88]. This demonstrates the long-time accuracy of our numerical calculations. For even dimensions of spacetime, we leave the analysis in Appendix.B.

#### IV. THE STABILITY ANALYSIS

In this section, we will perform the stability analysis from the perspective of both frequency and time domains. Due to their non-conservative nature, black hole systems are described by non-Hermitian operators. Unlike Hermitian operators, whose spectra fully characterize their properties, the spectra of non-Hermitian operators provide only partial information and are susceptible to potential instabilities [49, 89]. Non-Hermitian operators are characterized by pseudospectrum, which also captures the instability of their eigenvalues. Given  $\epsilon > 0$ , and a norm  $\|\cdot\|$ , the  $\epsilon$ -pseudospectrum for an operator  $A$  is defined as [49]

$$\sigma_\epsilon(A) = \{\omega \in \mathbb{C} : \|(A - \omega I)^{-1}\| > \epsilon^{-1}\}, \quad (4.1)$$



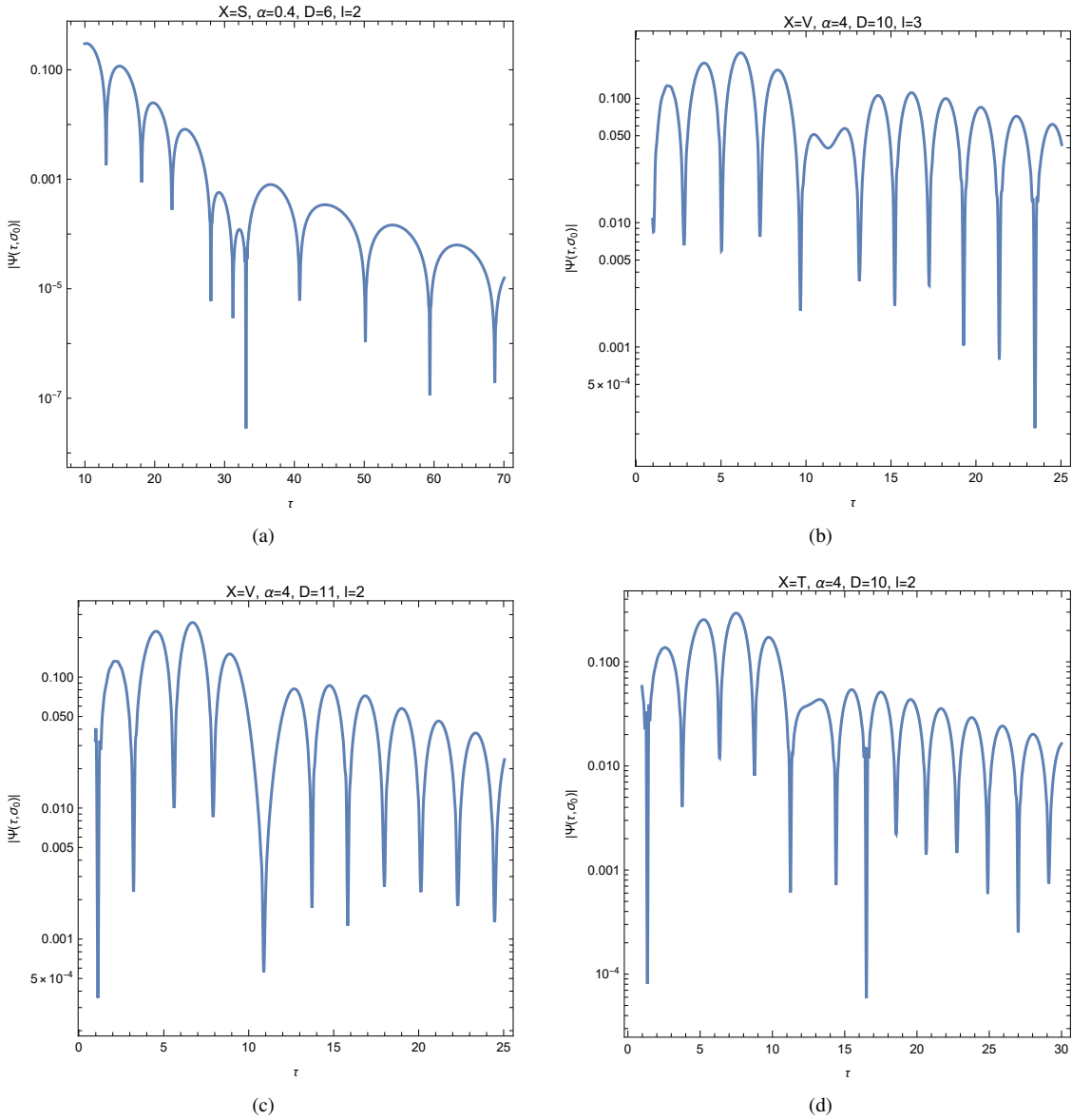


Figure 3: The zoomed-in view of Figs.2(j), 2(p), 2(r), and 2(z), where the rise phase followed after the first decay phase is illustrated. The parameters in Figs. 3(b), 3(c), and 3(d) are the same as those in Figs.2(p), 2(r), and 2(z) except the initial condition  $b_0 = 1/(10\sqrt{10})$  is changed as  $b_0 = 1/100$ .

where  $I$  is the identity operator,  $R_A(\omega) = (A - \omega I)^{-1}$  is called the resolvent operator. This definition is the most suitable for computing the pseudospectrum. Another equivalent and more intuitive definition of the pseudospectrum is [49]

$$\sigma_\epsilon(A) = \{\omega \in \mathbb{C} : \exists \delta A \text{ with } \|\delta A\| < \epsilon \text{ such that } \omega \in \sigma(A + \delta A)\}. \quad (4.2)$$

In the limit  $\epsilon \rightarrow 0$ , the set  $\sigma_\epsilon(A)$  reduces to the spectrum set  $\sigma(A)$ , whose elements are the spectrum  $\omega_n$ . The quantity  $\epsilon$  serves as a measure of the “proximity” between points in  $\sigma_\epsilon(A)$  and the spectrum  $\omega_n$ , offering a clear interpretation of perturbations to the underlying operator. The boundary of  $\sigma_\epsilon(A)$  is just the constant- $\epsilon$  contour. The choice of norm strongly affects the shape and structure of the pseudospectrum. Here, we choose the above norm to be the so-called energy norm [50, 90, 91]. For a function  $u(\sigma)$ , it is defined as

$$\|u\|_E = \sqrt{\langle u, u \rangle_E}, \quad (4.3)$$

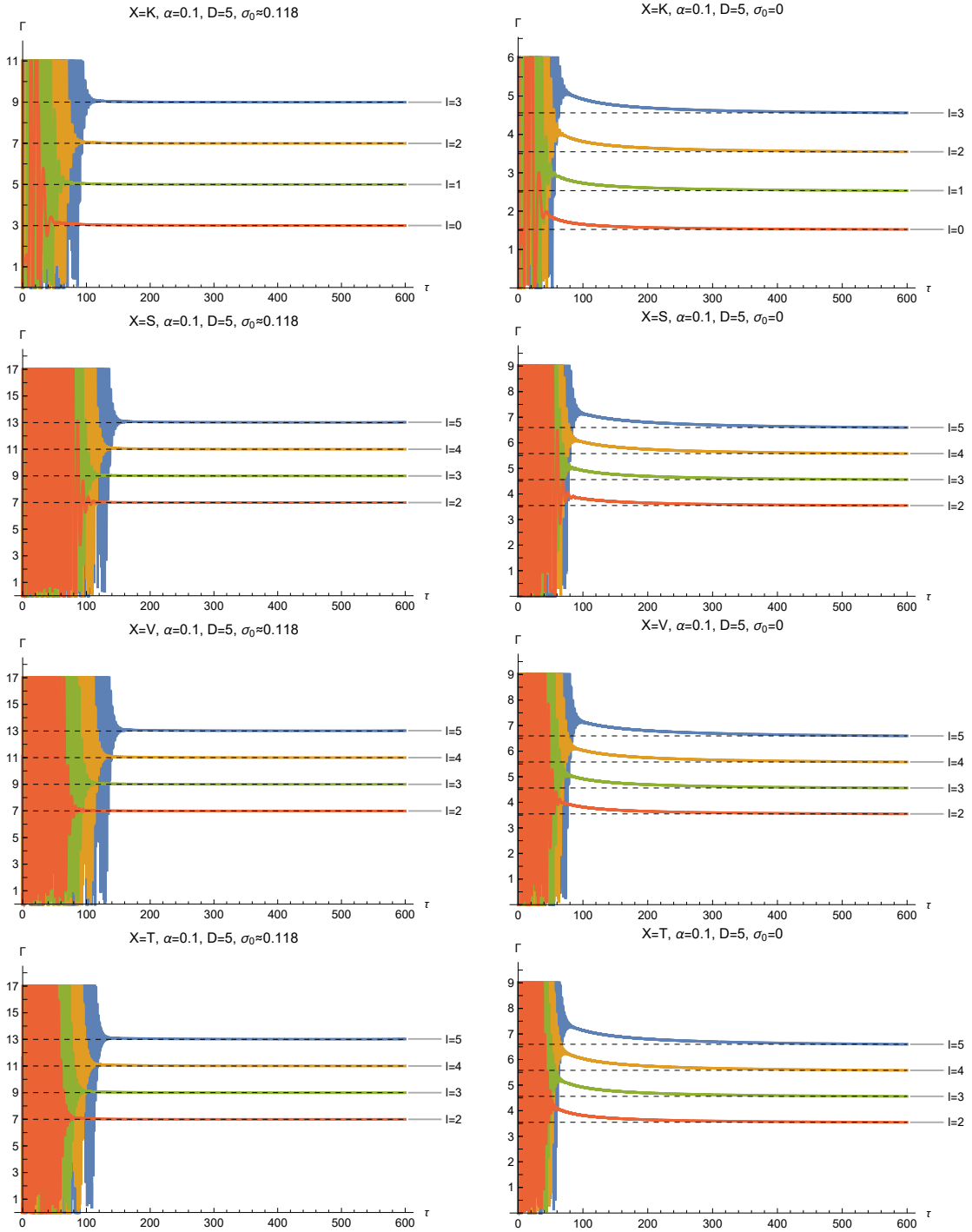


Figure 4: The effective power-law index  $\Gamma$  is computed using the initial conditions specified in Eqs.(3.7) with  $a_0 = 1, b_0 = 1/(10\sqrt{10})$  and  $c_0 = 1/5$ . The observer is located at  $\sigma_0 \approx 0.118$  in the first column and infinity, i.e.,  $\sigma_0 = 0$ , in the second column, with the computations performed on the resolution  $N = 300$  using time step  $\Delta\tau = 0.075$ .

which is induced by the energy inner product

$$\langle u_1, u_2 \rangle_E = \left\langle \begin{pmatrix} \Psi_1 \\ \Pi_1 \end{pmatrix}, \begin{pmatrix} \Psi_2 \\ \Pi_2 \end{pmatrix} \right\rangle_E = \frac{1}{2} \int_0^1 \left( w(\sigma) \bar{\Pi}_1 \Pi_2 + p(\sigma) \partial_\sigma \bar{\Psi}_1 \partial_\sigma \Psi_2 + q(\sigma) \bar{\Psi}_1 \Psi_2 \right) d\sigma, \quad (4.4)$$

where the bar represent the complex conjugate. In numerical computations, integrals (4.4) can be efficiently approximated using the Chebyshev-Lobatto grid and the Clenshaw-Curtis quadrature. This approach involves computing a weighted sum of the function values at the grid points, leading to an inner product that incorporates a Gram matrix  $\mathbf{G}$ . It means that Eq.(4.4) is

approximated by the following discrete version

$$\left\langle \begin{pmatrix} \Psi_1 \\ \Pi_1 \end{pmatrix}, \begin{pmatrix} \Psi_2 \\ \Pi_2 \end{pmatrix} \right\rangle_{\mathbf{E}} = (\Psi_1^* \ \Pi_1^*) \cdot \mathbf{G} \cdot \begin{pmatrix} \Psi_2 \\ \Pi_2 \end{pmatrix}, \quad (4.5)$$

where the asterisk denotes the Hermitian conjugate. With the help of the Gram matrix, the energy norm of any operator  $A$  is given by

$$\|A\|_{\mathbf{E}} = \|\mathbf{W} \cdot \mathbf{A} \cdot \mathbf{W}^{-1}\|_2 \quad (4.6)$$

where  $\mathbf{A}$  is the matrix approximation of the operator  $A$ ,  $\mathbf{W}$  is the Cholesky decomposition of  $\mathbf{G}$ , i.e.,  $\mathbf{G} = \mathbf{W}^* \cdot \mathbf{W}$  and  $\|\cdot\|_2$  represents the matrix 2-norm. For any point  $\omega$  in the complex plane (excluding the exact QNM spectra), the norm of the corresponding resolvent  $\|R_{L/i}(\omega)\|_{\mathbf{E}}$  can be calculated using Eq.(4.6) with  $A = R_{L/i}(\omega)$ . Given a positive constant  $\epsilon$ , the  $\epsilon$ -pseudospectrum of the operator  $L/i$ , i.e.,  $\sigma_{\epsilon}(L/i)$  is defined as the set of all  $\omega$  such that  $\|R_{L/i}(\omega)\|_{\mathbf{E}} > \epsilon^{-1}$  [see (4.1)]. In practice, we generate the contour plots using  $-\ln(\|1/R_{L/i}(\omega)\|_{\mathbf{E}})$ . Further computational details can be found in [50, 52, 78]. Unlike in general relativity, spacetimes in EGB gravity can possess (linear) unstable modes, resulting in a non-positive definite energy inner product that cannot define a norm. In addition to the above computational challenges, spacetimes exhibiting dynamic unstable modes is considered non-physical, rendering the analysis of QNM spectrum stability meaningless. Fig.5 presents the pseudospectrum corresponding to the parameters chosen in Fig.1 except for those parameters where dynamic unstable modes exist. Therefore, there are only 11 panels in Fig.5. The calculation is performed on resolution  $N = 100$ . The QNM spectra are computed with the same resolutions and they are represented by a black plus sign in each panel.

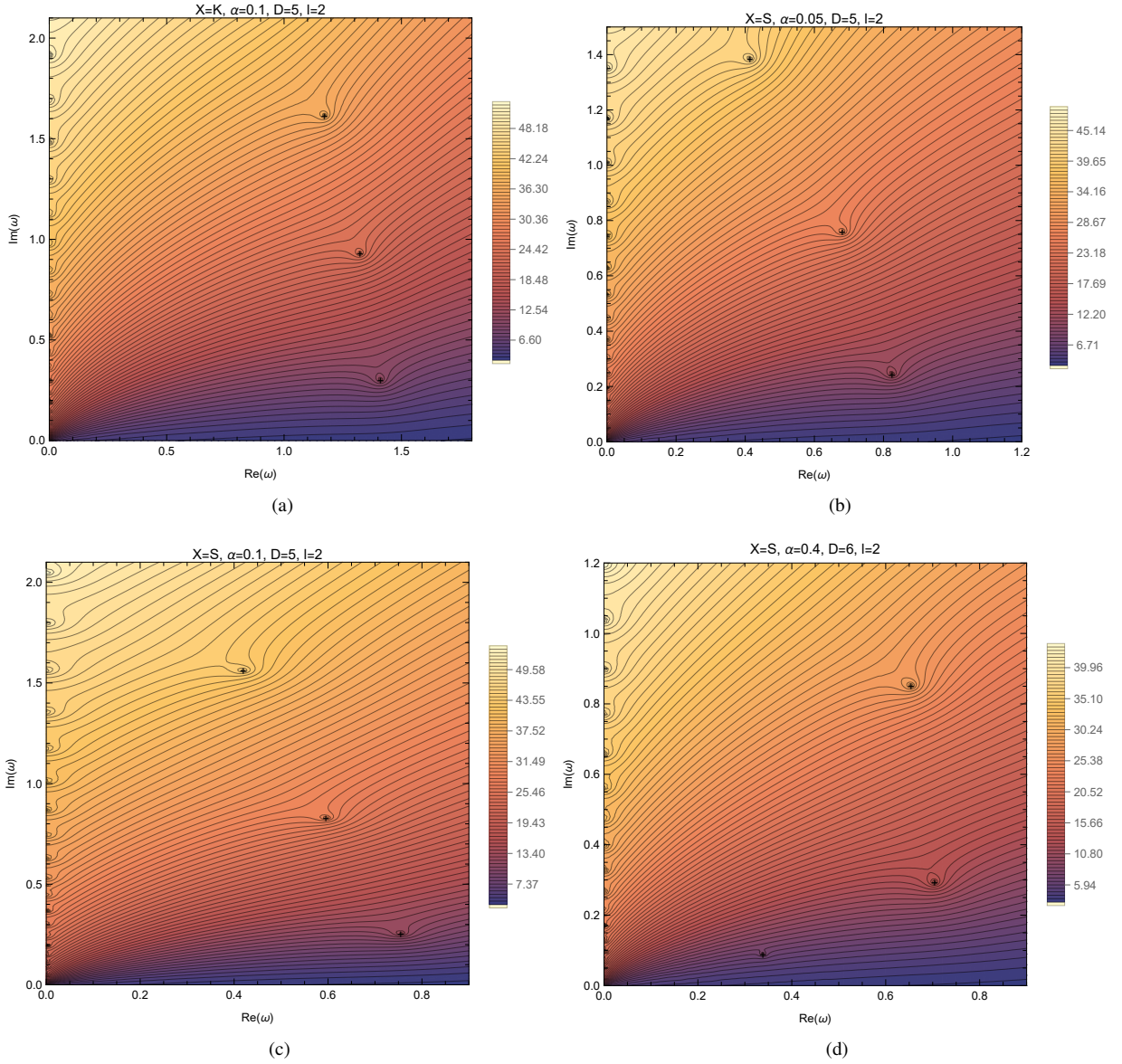
It can be read from Fig.5, when  $\omega$  is not in close proximity to a QNM spectrum,  $\|R_{L/i}(\omega)\|_{\mathbf{E}}$  increases with the increasing of the imaginary part of  $\omega$ . However, for those  $\omega$  in the vicinity of a QNM spectrum,  $\|R_{L/i}(\omega)\|_{\mathbf{E}}$  increases rapidly as  $\omega$  approaches the QNM spectrum. A perturbation with norm  $\epsilon$  displaces the QNM spectra from their original positions, with the  $\epsilon$ -pseudospectrum providing a bound on their displacement [see (4.2)]. For small  $\epsilon$ , the constant- $\epsilon$  contour line enclose the QNM spectrum, forming a closed curve. However, for slightly larger  $\epsilon$ , the constant- $\epsilon$  contour line extends well, forming an open structure that can even reach infinity. It suggests that perturbations of this magnitude may cause significant migration of the QNM spectrum. For each QNM spectrum, there exists a critical value  $\epsilon_c$  that separates closed contour lines from the open contour lines in the pseudospectrum. For perturbations with  $\epsilon < \epsilon_c$ , the QNM spectrum remains stable, while for  $\epsilon > \epsilon_c$ , the QNM spectrum can become highly unstable. A QNM spectrum's stability can be characterized by its critical value  $\epsilon_c$ , with larger values indicating greater stability. It can be seen that  $\epsilon_c$  decreases as the overtone number  $n$  increases, which demonstrates that higher overtones exhibit more spectrum instability.

In addition, in Figs.5(g), 5(h), and 5(k), we find each panels contain a branch of discrete spurious QNM spectra located near the imaginary axis. These QNM spectra, identified as spurious using the method described in Appendix A, originate from the branch cut of the Green function along the positive imaginary semi-axis, which causes the discrete matrix to capture a set of QNM spectra along this semi-axis. At low resolution, these QNM spectra detach from the axis, forming the observed spurious branches. As resolution increases, these spurious QNM spectra gradually return to the imaginary axis. This behavior is a characteristic feature of asymptotically flat spacetimes, and our model is no exception. In fact, the process of discreteness can also be regarded as perturbations to the original analytical system. Increasing the resolution essentially reduces such perturbation. Therefore, this reduction in perturbation causes spurious modes to progressively return to the imaginary axis, while simultaneously enhancing the convergence of the computed QNM spectra towards the true physical QNM spectra. More importantly, it still remains an open question whether the norm of resolvent of the matrix operator  $\mathbf{L}$  obtained from the hyperboloidal framework in asymptotically flat spacetime converges to the true norm of the resolvent of the original operator  $L$  as the resolution increases. Nonetheless, while the quantitative calculations of the resolvent may be under suspicion, the qualitative insights derived from these calculations remain valid [59].

As shown by the second definition of the pseudospectrum (4.2), considering the pseudospectra of  $\mathbf{L}/i$  is equivalent to consider any perturbation on the matrix, including those who could unphysically disturb the differential part of the operator  $L$ . True physical perturbations should be confined to alterations in the effective potential, potentially induced by surrounding matter in the environment. The preceding discussion focuses on the spectrum stability in the frequency domain. We now shift our attention to stability analysis in the time domain. In the following, we investigate the effects of specific perturbations on the effective potential in the time domain. Considering the potential impact of the surrounding environment on the black hole's effective potential, we introduce a specific bump in the potential to model this effect

$$\delta V(r(\sigma)) = a \left(1 - \frac{r_+}{r}\right)^2 \exp\left[-\frac{(r/r_+ - 1/c)^2}{2b^2}\right] = a(1 - \sigma)^2 \exp\left[-\frac{(1/\sigma - 1/c)^2}{2b^2}\right], \quad (4.7)$$

where  $a$  is the amplitude of  $\delta V$ ,  $c$  approximately represents the center of the bump in the  $\sigma$  coordinate, as  $r_+/c$  approximately gives the center of the bump in the  $r$  coordinate. The width of the bump in the  $r$  coordinate is characterized by  $br_+$ . Utilizing



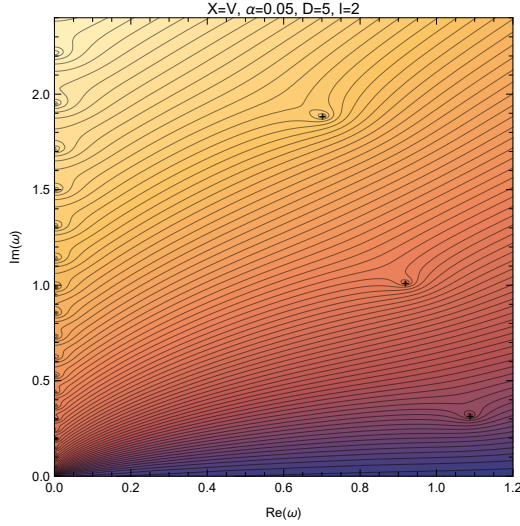
the relationship  $\sigma = r_+/r$ , we can estimate the width of the bump in the  $\sigma$  coordinate  $\Delta\tau$  as

$$\Delta\sigma = \frac{\Delta\sigma}{\Delta r} \Delta r = \left| \frac{d\sigma}{dr} \right|_{r=\xi} \Delta r = \frac{r_+}{\xi^2} br_+ \approx c^2 b, \quad (4.8)$$

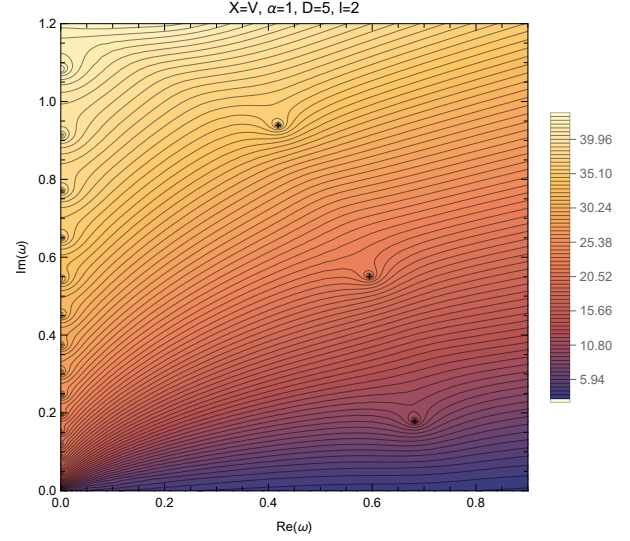
where in the second step, the Lagrange's mean value theorem guarantees the existence of  $\xi$ , and in the final step, we approximate  $\xi \approx r_+/c$ . Note that  $a, b, c$  should not be confused with the parameters  $a_0, b_0, c_0$  that characterize the initial waveform in Eqs.(3.7). The factor  $(1 - r_+/r)^2$  is included to prevent the disturbances near the horizon, while simultaneously maintaining the asymptotic behavior of the effective potential near the horizon. To quantify the time-domain impact of this perturbation, we calculate the mismatch between the time-domain signals generated by unperturbed and perturbed potentials observed at infinity ( $\sigma_0 = 0$ ) [92]. The mismatch between two time-domain signals,  $h_1(\tau)$  and  $h_2(\tau)$ , is defined as

$$\mathcal{M}(h_1, h_2) = 1 - \max_{\delta\tau} \frac{\langle h_1, h_2 \rangle}{\sqrt{\langle h_1, h_1 \rangle \langle h_2, h_2 \rangle}}, \quad (4.9)$$

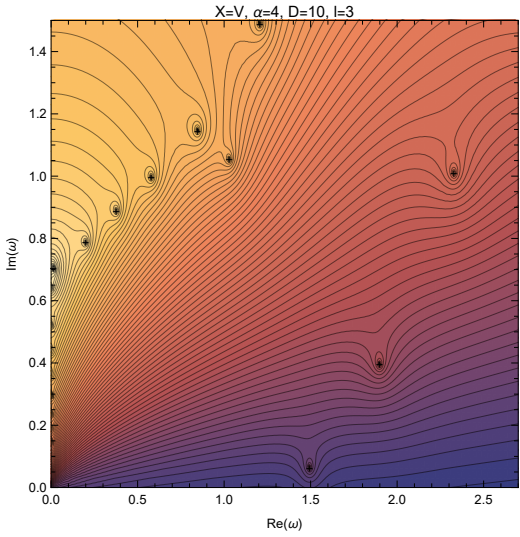
where we allow the waveform  $h_2$  to go through a time shift  $\delta\tau$ , and then maximize the inner product between  $h_1$  and shifted  $h_2$



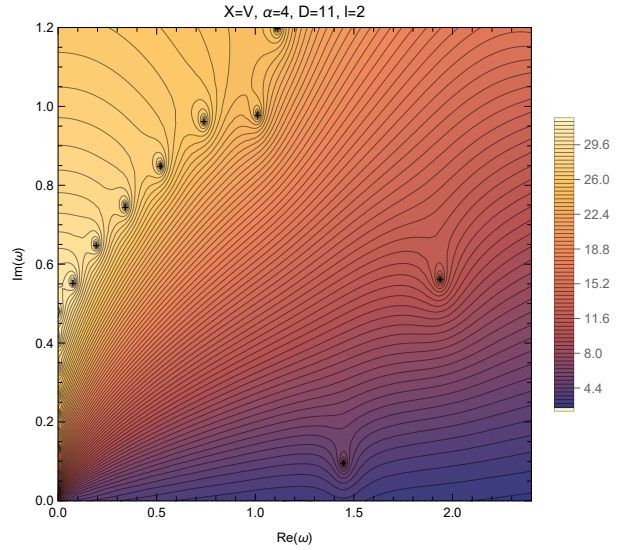
(e)



(f)



(g)



(h)

over  $\delta\tau$ , the inner product is defined as

$$\langle h_1, h_2 \rangle = 4 \operatorname{Re} \int_0^\infty \mathcal{F}\{h_1\}(\omega) \overline{\mathcal{F}\{h_2\}(\omega)} d\omega, \quad (4.10)$$

$\mathcal{F}\{\cdot\}$  indicates Fourier transformation and overbar denotes taking the complex conjugation. The shift  $\delta\tau$  in time is achieved by utilizing the time shift property of the Fourier transformation,

$$\mathcal{F}\{h_2(\tau + \delta\tau)\}(\omega) = e^{i\omega\delta\tau} \mathcal{F}\{h_2(\tau)\}(\omega). \quad (4.11)$$

$h_1$  and  $h_2$  are selected as the time-domain waveforms corresponding to the effective potentials before and after adding the bump seen by observers located at infinity. In numerical calculations, we work with values defined only at discrete time grid points. Consequently, we use the discrete Fourier transform (DFT) as an approximation of the true Fourier transform, and the vector inner product as an approximation of the integral. Same initial conditions are adopted to generate the signals. Waveforms are aligned in time such that their peaks coincide. After this alignment, it is observed that  $\delta\tau$  remains consistently small.

The norm rather than simply the amplitude  $a$  should be used to quantify the magnitude of the bump properly [93, 94]. The bump's norm is defined using the matrix norm from Eq.(4.6), specifically as the norm of the difference between the matrices  $L$

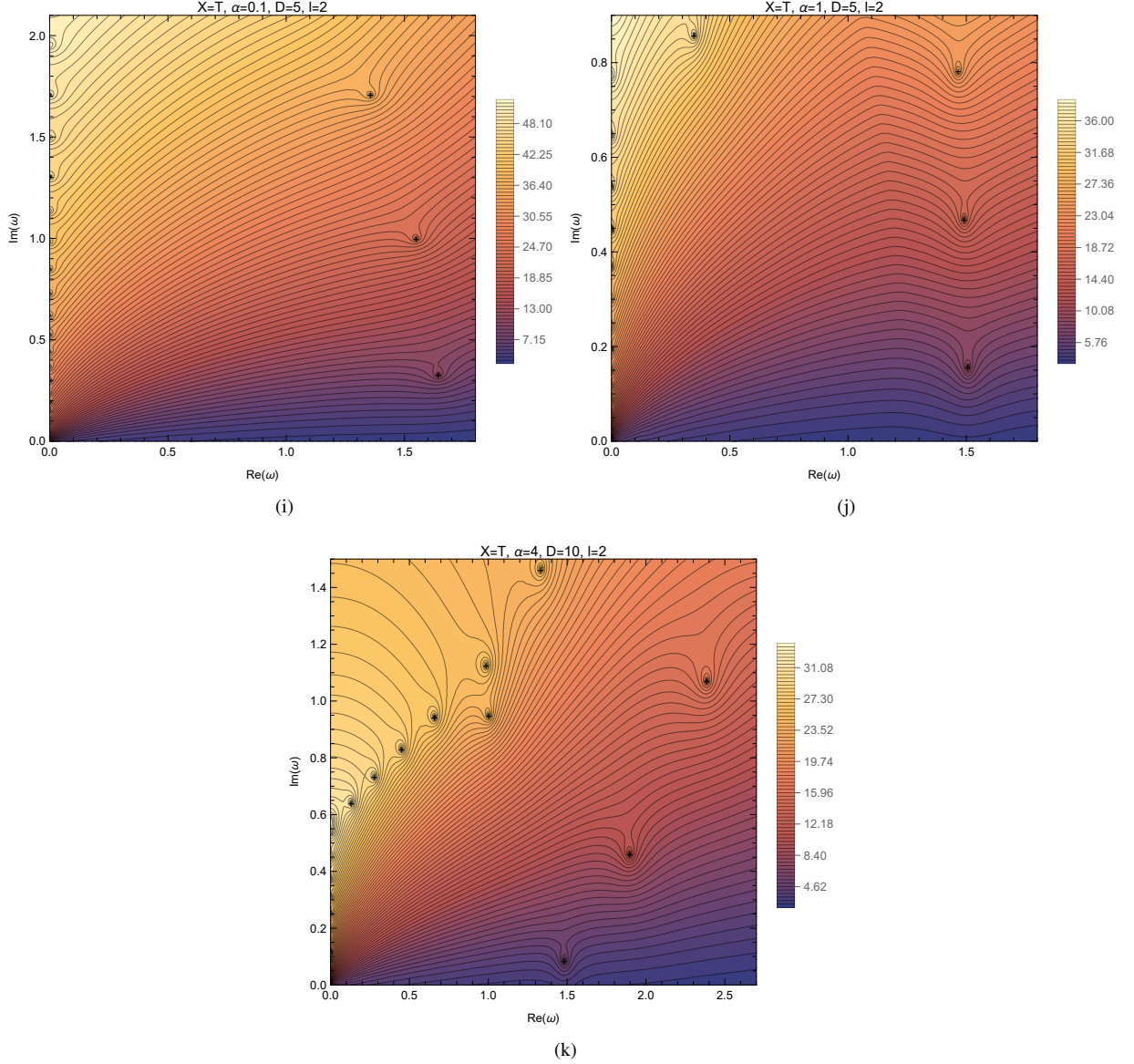


Figure 5: The contour plot of  $-\ln(1/\|(\mathbf{L}/i - \omega \mathbf{I})^{-1}\|_{\mathbb{E}})$  for the stable spacetime parameters in Fig.2. QNM spectra calculated using the same grid points and parameters is shown in each panel by a black plus sign. The calculation is performed on the resolution with  $N = 100$ .

from Eq.(2.13) constructed with and without the bump, i.e.,

$$\|\delta V\|_{\mathbb{E}} := \left\| \frac{1}{p(\sigma)w(\sigma)} \begin{pmatrix} 0 & 0 \\ \delta V(\sigma) & 0 \end{pmatrix} \right\|_{\mathbb{E}}, \quad (4.12)$$

where  $\delta V(\sigma)$  is given by Eq.(4.7) and its matrix representation is a diagonal matrix. Fig.6 illustrates that the bump's norm can vary dramatically despite a fixed amplitude  $a = 1$ , in which  $b$  is fixed as  $1/5$ . The norm satisfies  $\|a\delta V\|_{\mathbb{E}} = |a|\|\delta V\|_{\mathbb{E}}$ , so we simply fix  $a = 1$  in the Fig.6. As  $c$  approaches zero, the bump's position shifts further away from the black hole, resulting in its norm diverges which is in agreement with [94]. Simultaneously, the bump becomes increasingly narrow in the  $\sigma$  coordinate as shown in (4.8), making it more challenging for numerical discrete grids to capture its features accurately.

Fig.7 shows the relationship between the mismatch  $\mathcal{M}$  and the norm of the perturbation,  $\|\delta V\|_{\mathbb{E}}$ , for  $c = 1/10, 4/10, 7/10, 1$ . The width of the bump, which is determined by the parameter  $b$ , is fixed as  $1/5$ . The initial wave is Eqs.(3.7) with  $a_0 = 1, b_0 = 1/(10\sqrt{10})$  and  $c_0 = 1/5$ . For fixed  $c$ , the linear fit (dotted line) with a slope of approximately 2 indicates a quadratic relationship,  $\mathcal{M} \propto \|\delta V\|_{\mathbb{E}}^2$ . Since the mismatch cannot exceed 1, this quadratic relationship only holds when the norm of the perturbation is small enough. This demonstrates the stability of the time-domain waveform: small perturbations in the effective potential lead to proportionally smaller mismatches, implying a smooth, rather than abrupt, change in the waveform.

Fig.8 shows the relationship between the mismatch  $\mathcal{M}$  and the location of the perturbation, which is described by the param-

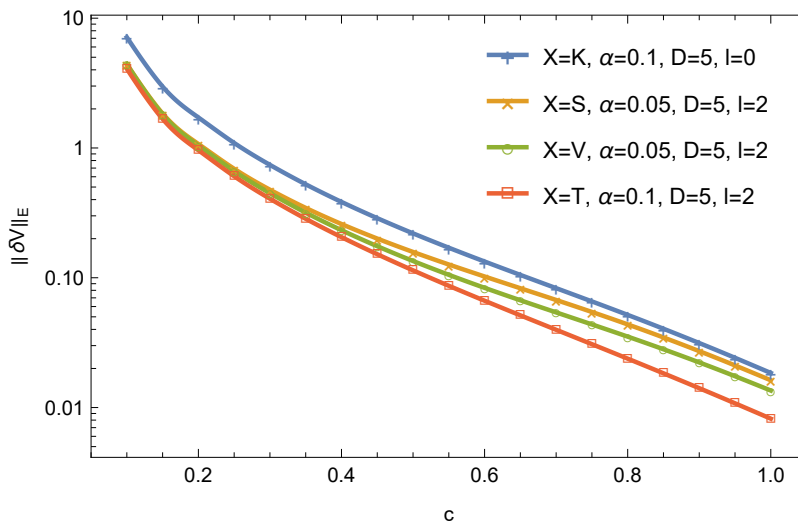


Figure 6: The  $\|\delta V\|_E$  for bump in Eq.(4.7) with different  $c$ ,  $b$  is fixed as  $1/5$  and  $a$  is fixed as 1. The computation is performed on a  $N = 200$  grid.

eter  $c$ , for  $\|\delta V\|_E = 10^{-4}, 10^{-3.5}, 10^{-3}, 10^{-2.5}, 10^{-2}, 10^{-1.5}, 10^{-1}$ . The width of the bump is fixed as  $b = 1/5$ . The initial wave is chosen to be Eqs.(3.7) with  $a_0 = 1, b_0 = 1/(10\sqrt{10})$  and  $c_0 = 1/5$ . The line connecting points with the same norm is determined through fitting. Fig.8 presents a comprehensive view of the data, which is partially shown in Fig.7. Due to the small magnitude of differences between different sets of the data, plotting all data points in Fig.7 results in significant overlap. Therefore, Fig.7 displays only four representative datasets. For a fixed  $\|\delta V\|_E$ , the position of the bump has minimal impact. We present Fig.7 and Fig.8 with a different initial condition in Appendix.C, where  $c_0 = 1/5$  is replaced by  $c_0 = 4/5$ . The linear fits in Fig.11 and Fig.7 exhibit slopes of approximately 2, demonstrating that time-domain stability is independent of the initial conditions.

## V. CONCLUSIONS AND DISCUSSION

In this paper, we explore the QNMs and their (in)stability of BDW black holes within the framework of EGB gravity theory in both frequency domain and time domain using the hyperboloidal formalism. The effective potential of gravitational perturbations in BDW black holes exhibits a variety of shapes depending on the parameters. These potentials can display single or double peaks and may also feature negative regions, either adjacent to or distant from the event horizon. Such variations in the effective potential are inherent to the theoretical framework and are not the result of artificial perturbations or external conditions. Additional perturbations could lead to even more complex configurations. We calculated the QNMs for these typical effective potentials in both the frequency and time domains, identifying characteristic QNMs such as echoes and instabilities. Spurious modes, arising from numerical artifacts, are eliminated through joint computation at multiple resolutions. We further validated our code by computing the Price's law. Our results align with the expected behavior in odd spacetime dimensions, but we found limited evidence supporting the Price's law in even dimensions, similar to the findings of Abdalla *et al.* [70].

The (in)stability of QNMs in frequency domain is assessed by calculating the pseudospectrum. The  $\epsilon$ -pseudospectrum provides an upper bound on the migration of QNM spectra induced by a perturbation to the effective potential with a norm of  $\epsilon$ . However, certain parameter configurations of spacetimes reveal dynamically unstable QNMs, indicated by a negative imaginary part. This instability leads to energy inner products that are not positive definite. As a result, one cannot define an energy norm or calculate the pseudospectrum. From a physical perspective, the stability of QNMs and pseudospectrum in unstable spacetimes is also meaningless. The pseudospectrum accounts for arbitrary perturbations on the time-evolving operator, including those that may be unphysical, e.g., changing the structure of the derivative part. However, even within its limitations, [50] suggests that high-frequency perturbations on the effective potential can possibly saturate this upper bound given by pseudospectrum. In numerical computations of asymptotically flat spacetimes using hyperboloidal formalism, finite-rank approximations of the resolvent operator  $R_{L/i}(\omega)$  may exhibit quantitative inaccuracies but do capture the qualitative features of the pseudospectrum.

The (in)stability of QNMs in time domain are studied by compare the waveforms evolved before and after adding a bump on effective potential. We use mismatch to quantify the difference between the two waveforms. Results shows that for a bump with small norm on the effective potential, the mismatch remains small and scales quadratically with the bump's norm. This indicates that the waveform is robust against perturbations on the effective potential. The apparent contradiction between frequency instability and time domain stability requires further investigation.

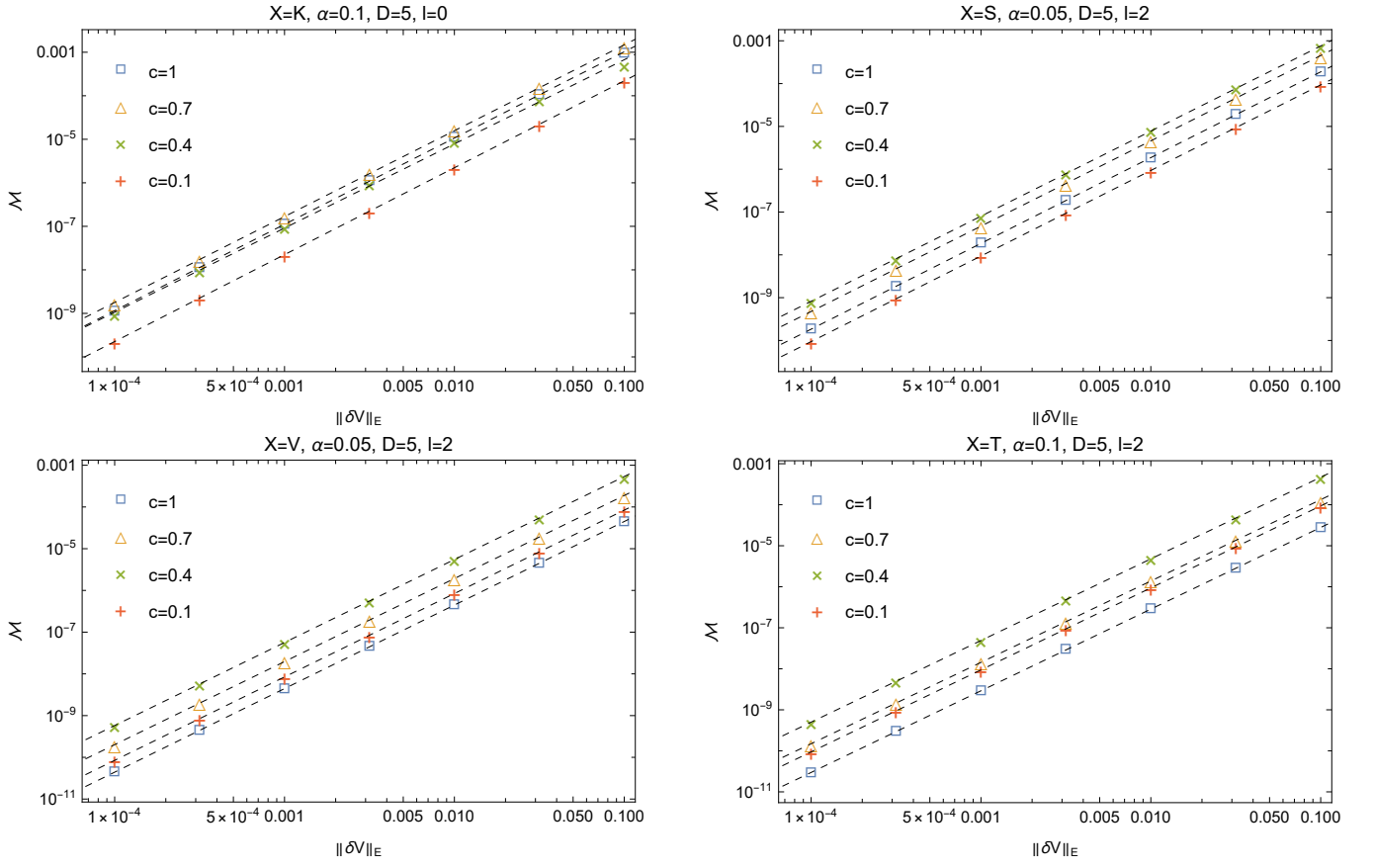


Figure 7: The relationship between mismatch  $\mathcal{M}$  and  $\|\delta V\|_E$  for different  $c$  values of the bump. The width  $b$  of the bump is fixed as  $1/5$ . The initial wave is chosen to be Eqs.(3.7) with  $a_0 = 1, b_0 = 1/(10\sqrt{10})$  and  $c_0 = 1/5$ . The dashed lines represent the fitted lines, which have slopes of approximately 2. The computation is performed on a  $N = 200$  grid using time step  $\Delta\tau = 0.075$ .

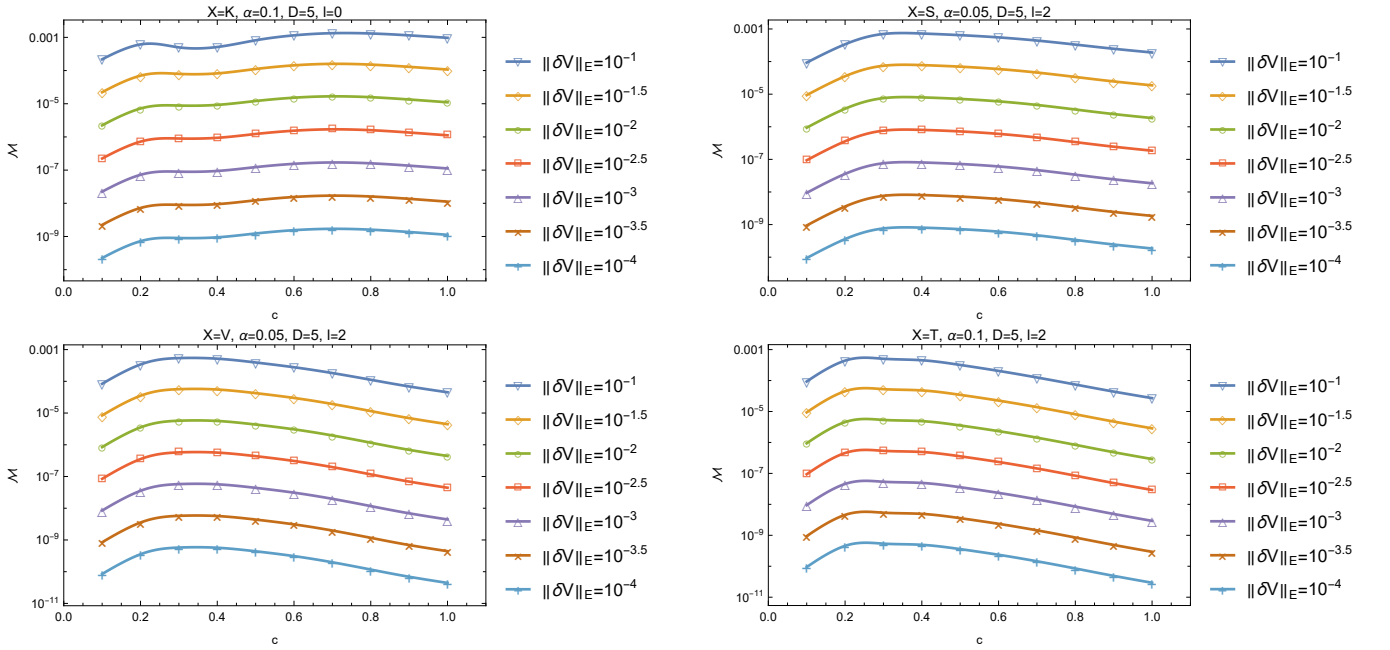


Figure 8: The relationship between mismatch  $\mathcal{M}$  and the location of the bump, which is described by the parameter  $c$ , for varies norm  $\|\delta V\|_E$ . The width of the bump  $b$  is fixed as  $1/5$ . The initial wave is specified as Eqs.(3.7) with  $a_0 = 1, b_0 = 1/(10\sqrt{10})$  and  $c_0 = 1/5$ . The computation is performed on a  $N = 200$  grid using time step  $\Delta\tau = 0.075$ .



### Acknowledgement

This work was supported in part by the National Natural Science Foundation of China with grants No.12075232 and No.12247103.

### Appendix A: Criteria for identifying physically relevant QNMs

Identifying true physical QNMs from contaminated ones requires careful inspection. A common strategy is to examine whether the calculated modes converge to a fixed point as the grid resolution increases, or alternatively, if they align with previously computed modes. For a given grid resolution  $N$  associated with eigenvalues  $\omega_i, i = 1, 2, \dots, n$ , we define a drift ratio relative to another higher resolution  $N_1$ ,

$$r_i^{(N_1)} = \frac{\min\{|\omega_i|, \sigma_i\}}{\delta_i^{(N_1)}}, \quad (\text{A1})$$

where the intermodal separation  $\sigma_i$  is,

$$\sigma_i = \begin{cases} |\omega_1 - \omega_2|, & i = 1, \\ \frac{1}{2}(|\omega_i - \omega_{i-1}| + |\omega_{i+1} - \omega_i|), & 1 < i < n, \\ |\omega_{n-1} - \omega_n|, & i = n, \end{cases} \quad (\text{A2})$$

the nearest neighbor drift is,

$$\delta_i^{(N_1)} = \min_j |\omega_i - \omega_j^{(N_1)}|, \quad (\text{A3})$$

and  $\omega_i^{(N_1)}$  are eigenvalues of resolution  $N_1$ . Therefore, the eigenvalues corresponding to a physical mode will exhibit a significant drift ratio, whereas the numerical spurious eigenvalues rely heavily on resolution and show smaller drift ratios. To avoid potential coincidences between spurious eigenvalues at the resolutions  $N$  and  $N_1$ , we compute  $r_i^{(N_1)}$  and  $r_i^{(N_2)}$  with  $N_2 > N_1 > N$ . Only modes  $\omega_i$  that satisfy  $\min\{r_i^{(N_1)}, r_i^{(N_2)}\} > 10^3$  are considered good approximations of true physical QNMs. In asymptotically flat spacetimes, the branch cut along the positive imaginary axis leads to a continuous spectrum in this region. Consequently, there are a series of discrete modes located in this region for numerical computation, therefore we excluded modes in this region from the calculation of the drift ratio.

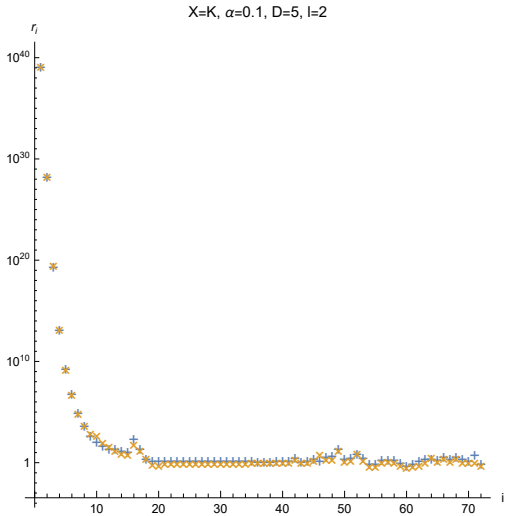
### Appendix B: Price's law in even dimensions

For observers at finite locations in even dimensions spacetimes, [84, 85] indicate that there exist power-law tail with index  $3D - 8$  (when  $X = K$  and  $l = 0$ ), or provide a lower bound on the index of  $2D - 5 + 2l$ . However, in [70], they did not observe a power-law tail for even dimensions. Fig.10 shows our computational results for observers located both in finite distance and infinity in even dimensions, where power-law tails emerge, but their indexes differs from the analytical predictions.

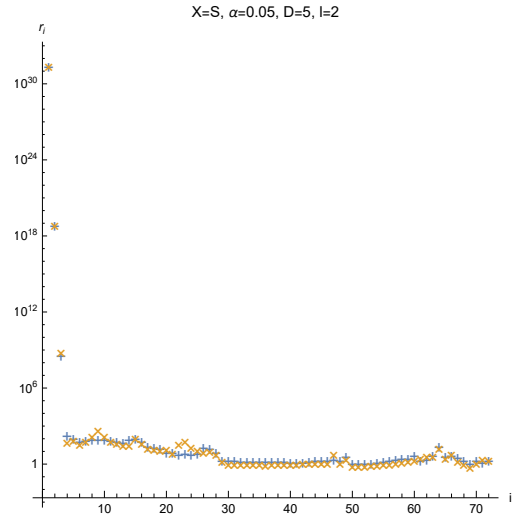
### Appendix C: Mismatch with different initial condition

In this appendix, we show the results of the relationship between mismatch and the width and the location of the bump with a different initial condition in Figs.11 and 12. The linear fits in Fig.11 and Fig.7 have slopes of approximately 2, indicating that time-domain stability is independent of the initial data.

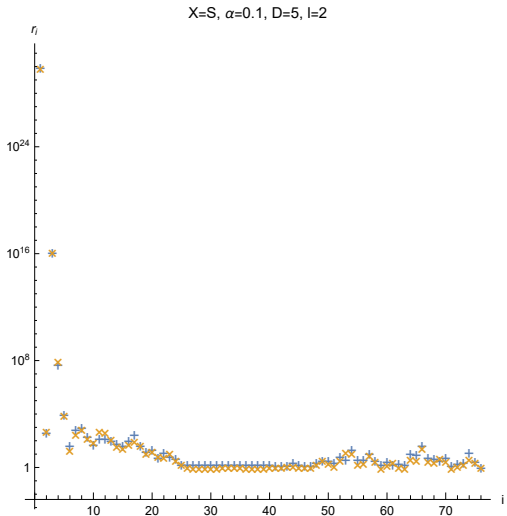
- 
- [1] S. B. Giddings and S. D. Thomas, *Phys. Rev. D* **65**, 056010 (2002), arXiv:hep-ph/0106219 .
  - [2] S. B. Giddings and M. L. Mangano, *Phys. Rev. D* **78**, 035009 (2008), arXiv:0806.3381 [hep-ph] .
  - [3] R. Emparan and H. S. Reall, *Living Rev. Rel.* **11**, 6 (2008), arXiv:0801.3471 [hep-th] .
  - [4] S. Dimopoulos and G. L. Landsberg, *Phys. Rev. Lett.* **87**, 161602 (2001), arXiv:hep-ph/0106295 .
  - [5] P. Kanti, *Int. J. Mod. Phys. A* **19**, 4899 (2004), arXiv:hep-ph/0402168 .
  - [6] I. Antoniadis, N. Arkani-Hamed, S. Dimopoulos, and G. R. Dvali, *Phys. Lett. B* **436**, 257 (1998), arXiv:hep-ph/9804398 .
  - [7] L. Randall and R. Sundrum, *Phys. Rev. Lett.* **83**, 3370 (1999), arXiv:hep-ph/9905221 .



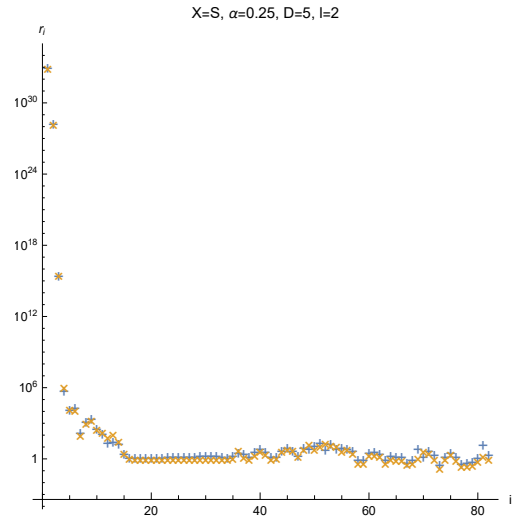
(a)



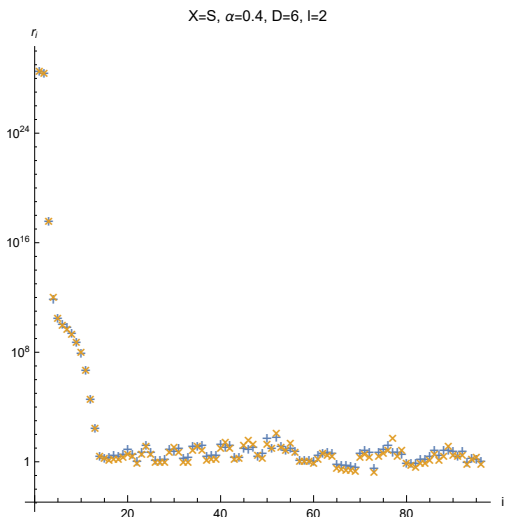
(b)



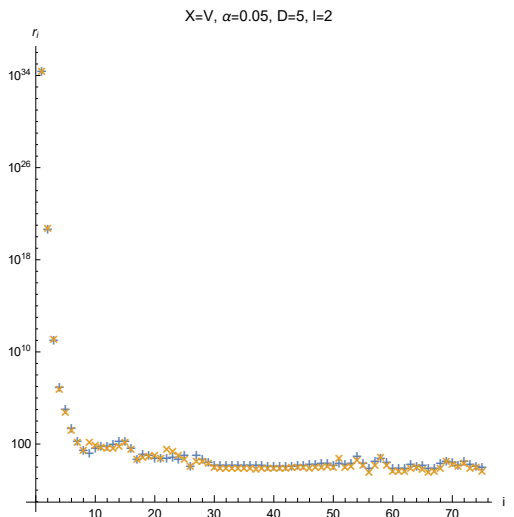
(c)



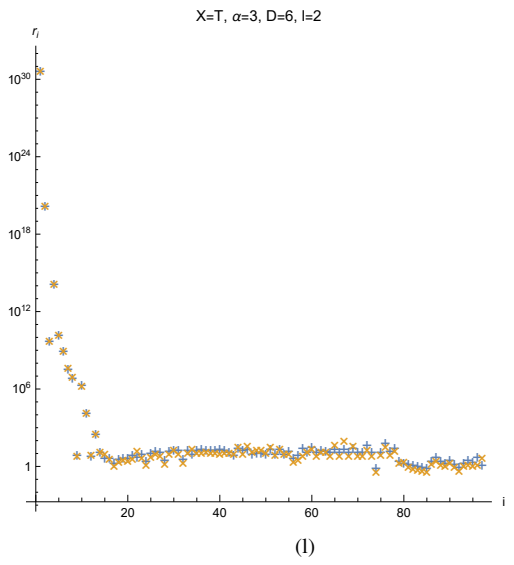
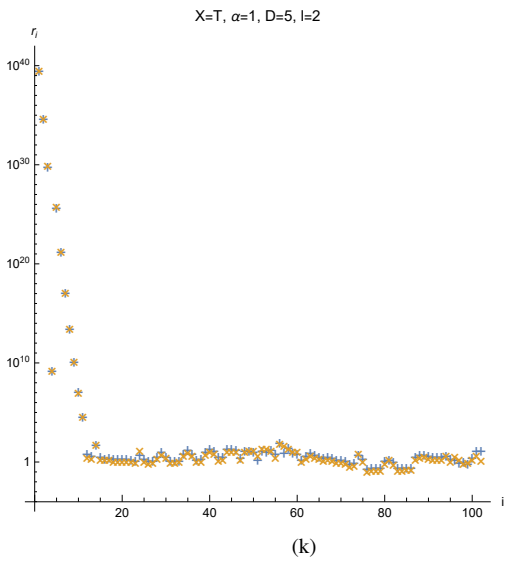
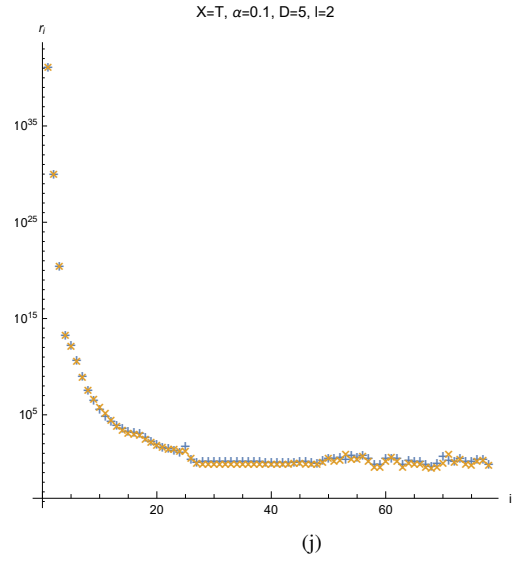
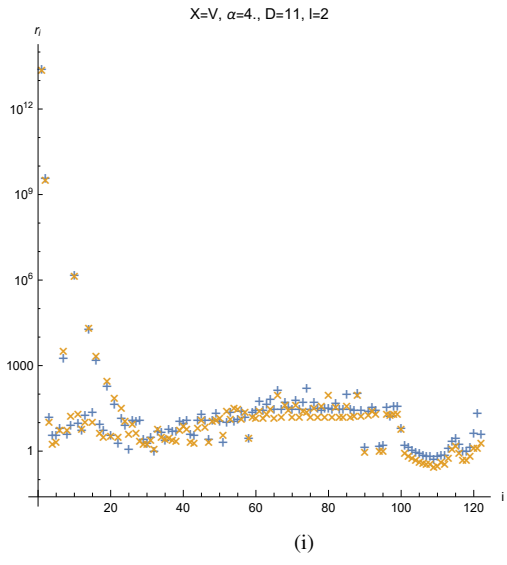
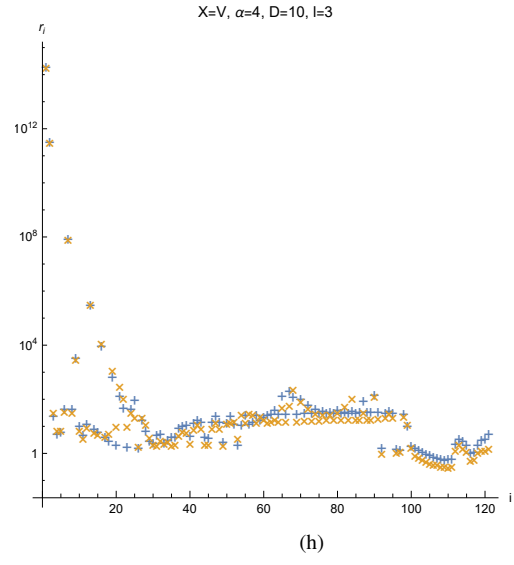
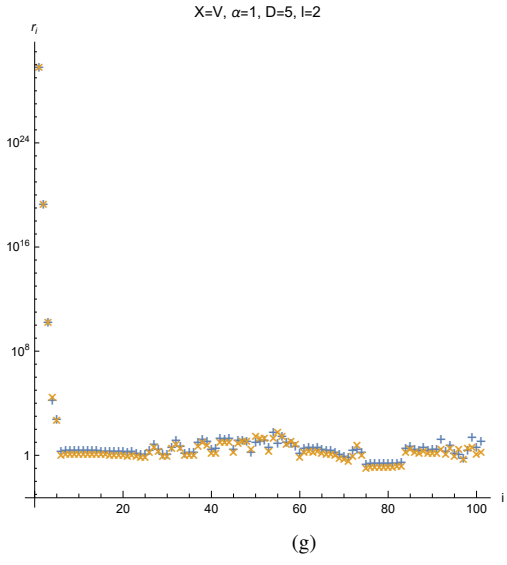
(d)



(e)



(f)



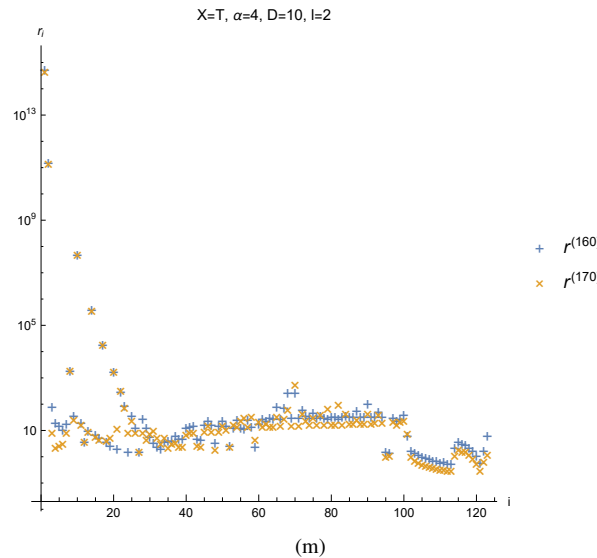


Figure 9: The drift ratio for the parameter choice in Fig.1. The calculation is performed on a grid with  $N = 150$ .

- [8] N. Arkani-Hamed, S. Dimopoulos, and G. R. Dvali, *Phys. Rev. D* **59**, 086004 (1999), arXiv:hep-ph/9807344 .
- [9] N. Arkani-Hamed, S. Dimopoulos, and G. R. Dvali, *Phys. Lett. B* **429**, 263 (1998), arXiv:hep-ph/9803315 .
- [10] C. Charmousis, *Lect. Notes Phys.* **769**, 299 (2009), arXiv:0805.0568 [gr-qc] .
- [11] T. Clifton, P. G. Ferreira, A. Padilla, and C. Skordis, *Phys. Rept.* **513**, 1 (2012), arXiv:1106.2476 [astro-ph.CO] .
- [12] D. Lovelock, *J. Math. Phys.* **12**, 498 (1971).
- [13] D. Lovelock, *J. Math. Phys.* **13**, 874 (1972).
- [14] B. Zwiebach, *Phys. Lett. B* **156**, 315 (1985).
- [15] D. J. Gross and E. Witten, *Nucl. Phys. B* **277**, 1 (1986).
- [16] D. G. Boulware and S. Deser, *Phys. Rev. Lett.* **55**, 2656 (1985).
- [17] J. T. Wheeler, *Nucl. Phys. B* **268**, 737 (1986).
- [18] R.-G. Cai, *Phys. Rev. D* **65**, 084014 (2002), arXiv:hep-th/0109133 .
- [19] R.-G. Cai and Q. Guo, *Phys. Rev. D* **69**, 104025 (2004), arXiv:hep-th/0311020 .
- [20] M. Brigante, H. Liu, R. C. Myers, S. Shenker, and S. Yaida, *Phys. Rev. Lett.* **100**, 191601 (2008), arXiv:0802.3318 [hep-th] .
- [21] M. Brigante, H. Liu, R. C. Myers, S. Shenker, and S. Yaida, *Phys. Rev. D* **77**, 126006 (2008), arXiv:0712.0805 [hep-th] .
- [22] M. Cvetič, S. Nojiri, and S. D. Odintsov, *Nucl. Phys. B* **628**, 295 (2002), arXiv:hep-th/0112045 .
- [23] H. Maeda and M. Nozawa, *Phys. Rev. D* **78**, 024005 (2008), arXiv:0803.1704 [gr-qc] .
- [24] L.-M. Cao, L.-B. Wu, Y. Zhao, and Y.-S. Zhou, *Phys. Rev. D* **108**, 124023 (2023).
- [25] S. Chandrasekhar, *The Mathematical Theory of Black Holes*, International series of monographs on physics (Clarendon Press, 1998).
- [26] H.-P. Nollert, *Class. Quant. Grav.* **16**, R159 (1999).
- [27] K. D. Kokkotas and B. G. Schmidt, *Living Rev. Rel.* **2**, 2 (1999), arXiv:gr-qc/9909058 .
- [28] E. Berti, V. Cardoso, and A. O. Starinets, *Class. Quant. Grav.* **26**, 163001 (2009), arXiv:0905.2975 [gr-qc] .
- [29] R. A. Konoplya and A. Zhidenko, *Rev. Mod. Phys.* **83**, 793 (2011), arXiv:1102.4014 [gr-qc] .
- [30] E. W. Leaver, *Phys. Rev. D* **34**, 384 (1986).
- [31] R. H. Price, *Phys. Rev. D* **5**, 2419 (1972).
- [32] R. H. Price, *Phys. Rev. D* **5**, 2439 (1972).
- [33] V. Baibhav, M. H.-Y. Cheung, E. Berti, V. Cardoso, G. Carullo, R. Cotesta, W. Del Pozzo, and F. Duque, *Phys. Rev. D* **108**, 104020 (2023), arXiv:2302.03050 [gr-qc] .
- [34] M. Giesler, M. Isi, M. A. Scheel, and S. Teukolsky, *Phys. Rev. X* **9**, 041060 (2019), arXiv:1903.08284 [gr-qc] .
- [35] B. P. Abbott et al. (LIGO Scientific, Virgo), *Phys. Rev. Lett.* **116**, 061102 (2016), arXiv:1602.03837 [gr-qc] .
- [36] E. Berti, K. Yagi, H. Yang, and N. Yunes, *Gen. Rel. Grav.* **50**, 49 (2018), arXiv:1801.03587 [gr-qc] .
- [37] M. Maggiore, *Gravitational Waves: Volume 2: Astrophysics and Cosmology* (Oxford University Press, 2018).
- [38] A. Zenginoglu, *Class. Quant. Grav.* **25**, 145002 (2008), arXiv:0712.4333 [gr-qc] .
- [39] A. Zenginoglu, *Phys. Rev. D* **83**, 127502 (2011), arXiv:1102.2451 [gr-qc] .
- [40] R. Panosso Macedo, *Phil. Trans. Roy. Soc. Lond. A* **382**, 20230046 (2024), arXiv:2307.15735 [gr-qc] .
- [41] A. Zenginoğlu, *Am. J. Phys.* **92**, 965 (2024), arXiv:2404.01528 [gr-qc] .
- [42] R. Panosso Macedo and A. Zenginoglu, (2024), arXiv:2409.11478 [gr-qc] .
- [43] E. Barausse, V. Cardoso, and P. Pani, *Phys. Rev. D* **89**, 104059 (2014), arXiv:1404.7149 [gr-qc] .
- [44] H.-P. Nollert, *Phys. Rev. D* **53**, 4397 (1996), arXiv:gr-qc/9602032 .
- [45] H.-P. Nollert and R. H. Price, *J. Math. Phys.* **40**, 980 (1999), arXiv:gr-qc/9810074 .
- [46] R. G. Daghigh, M. D. Green, and J. C. Morey, *Phys. Rev. D* **101**, 104009 (2020), arXiv:2002.07251 [gr-qc] .
- [47] W.-L. Qian, K. Lin, C.-Y. Shao, B. Wang, and R.-H. Yue, *Phys. Rev. D* **103**, 024019 (2021), arXiv:2009.11627 [gr-qc] .
- [48] K. Destounis and F. Duque (2023) arXiv:2308.16227 [gr-qc] .

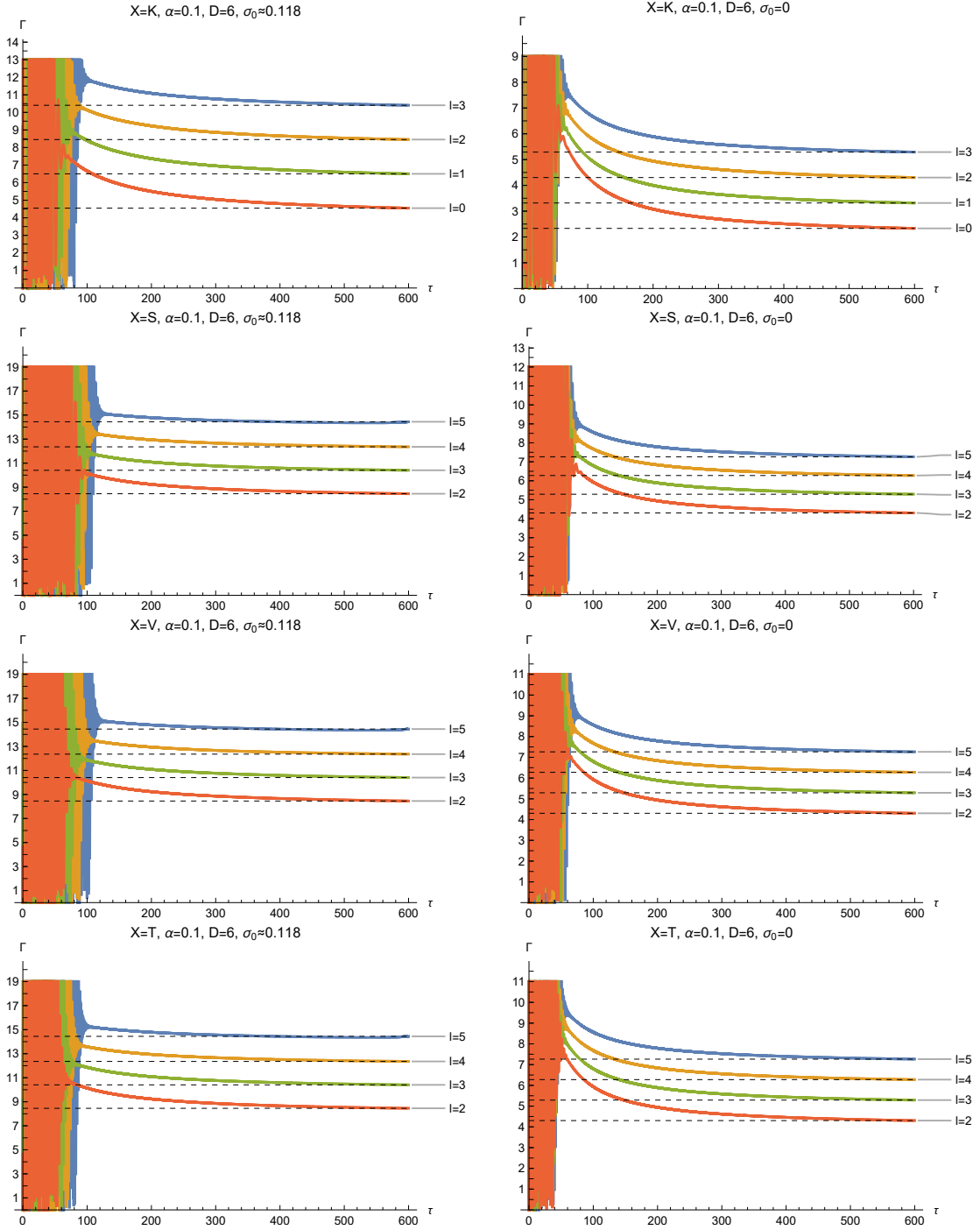


Figure 10: The effective power-law index  $\Gamma$  is computed using the initial conditions specified in Eqs.(3.7) with  $a_0 = 1$ ,  $b_0 = 1/(10\sqrt{10})$  and  $c_0 = 1/5$ . The observer is located at  $\sigma_0 \approx 0.118$  in the first column and infinity, i.e.,  $\sigma_0 = 0$ , in the second column, with the computations performed on the resolution  $N = 300$  using time step  $\Delta\tau = 0.075$ .

- [49] L. Trefethen and M. Embree, [Spectra and Pseudospectra: The Behavior of Nonnormal Matrices and Operators](#) (Princeton university press, 2005).
- [50] J. L. Jaramillo, R. Panosso Macedo, and L. Al Sheikh, *Phys. Rev. X* **11**, 031003 (2021), [arXiv:2004.06434 \[gr-qc\]](#).
- [51] K. Destounis, R. P. Macedo, E. Berti, V. Cardoso, and J. L. Jaramillo, *Phys. Rev. D* **104**, 084091 (2021), [arXiv:2107.09673 \[gr-qc\]](#).
- [52] L.-M. Cao, J.-N. Chen, L.-B. Wu, L. Xie, and Y.-S. Zhou, *Sci. China Phys. Mech. Astron.* **67**, 100412 (2024), [arXiv:2401.09907 \[gr-qc\]](#).
- [53] S. Sarkar, M. Rahman, and S. Chakraborty, *Phys. Rev. D* **108**, 104002 (2023), [arXiv:2304.06829 \[gr-qc\]](#).
- [54] K. Destounis, V. Boyanov, and R. Panosso Macedo, *Phys. Rev. D* **109**, 044023 (2024), [arXiv:2312.11630 \[gr-qc\]](#).
- [55] S. Luo, *Phys. Rev. D* **110**, 084071 (2024), [arXiv:2408.08139 \[gr-qc\]](#).

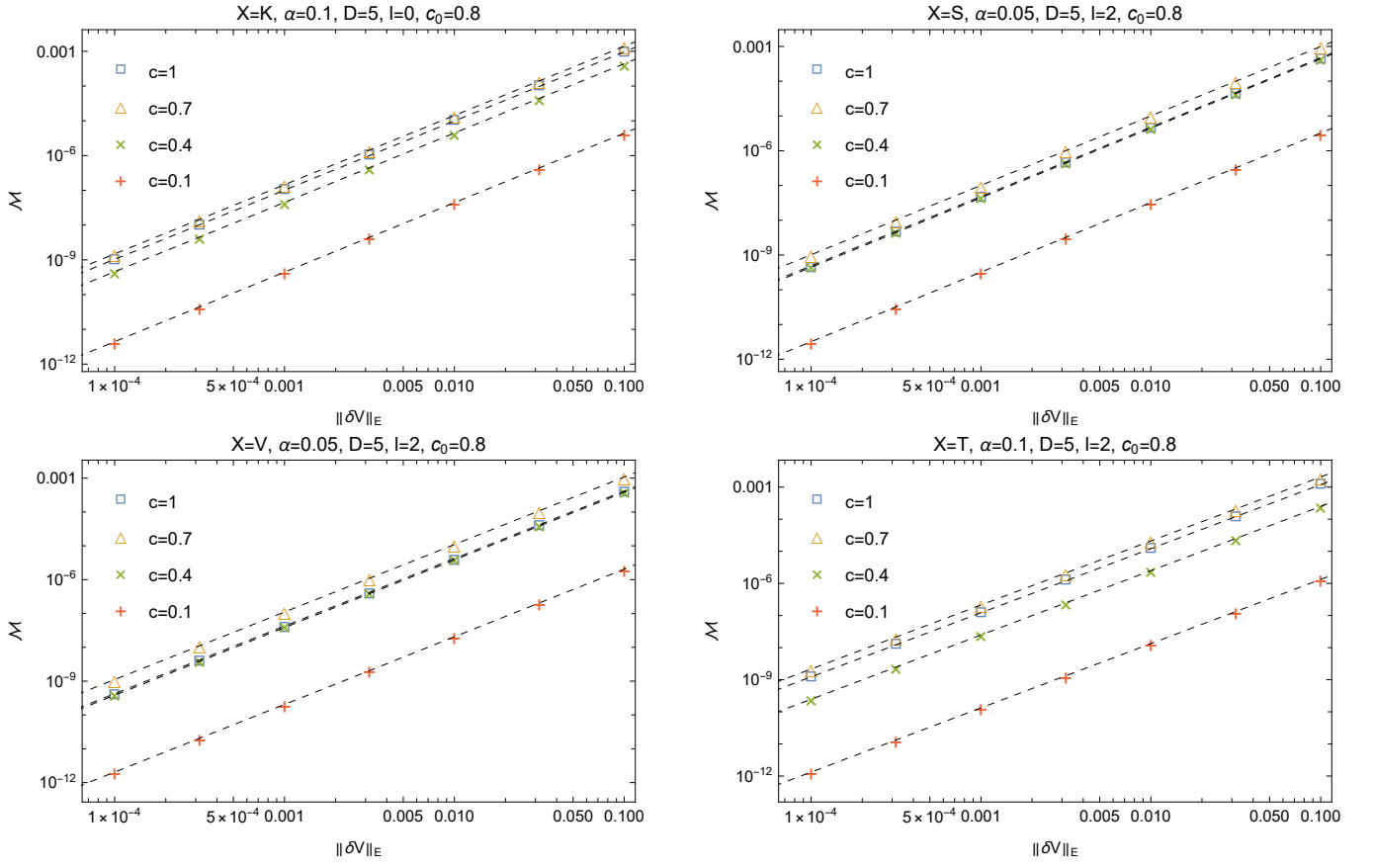


Figure 11: The relationship between mismatch  $\mathcal{M}$  and  $\|\delta V\|_E$  for different  $c$  values of the bump. The width  $b$  of the bump is fixed as  $1/5$ . The initial wave is chosen to be Eqs.(3.7) with  $a_0 = 1$ ,  $b_0 = 1/(10\sqrt{10})$  and  $c_0 = 4/5$ . The dashed lines represent the fitted lines, which have slopes of approximately 2. The computation is performed on a  $N = 200$  grid using time step  $\Delta\tau = 0.075$ .

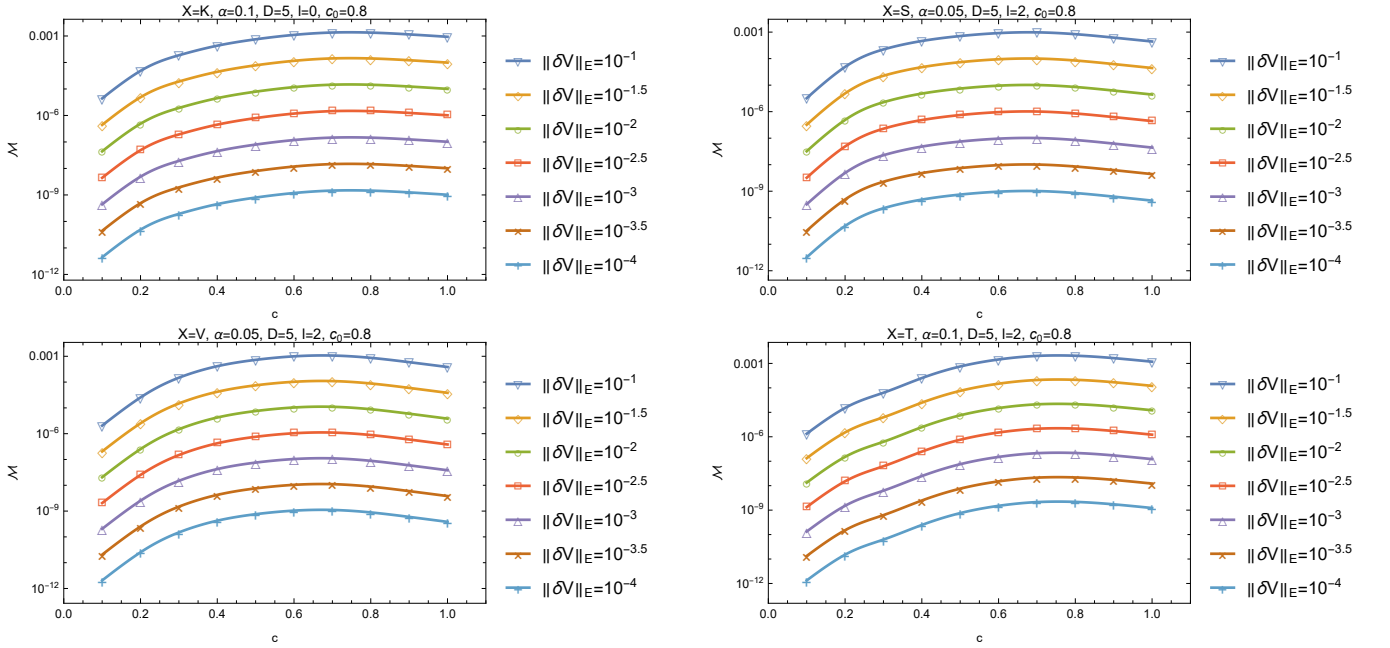


Figure 12: The relationship between mismatch  $\mathcal{M}$  and the location of the bump, which is described by the parameter  $c$ , for varies norm  $\|\delta V\|_E$ . The width of the bump  $b$  is fixed as  $1/5$ . The initial wave is specified as Eqs.(3.7) with  $a_0 = 1$ ,  $b_0 = 1/(10\sqrt{10})$  and  $c_0 = 4/5$ . The computation is performed on a  $N = 200$  grid using time step  $\Delta\tau = 0.075$ .

- [56] C. Warnick, (2024), [arXiv:2407.19850 \[gr-qc\]](#) .
- [57] D. Arean, D. Garcia-Fariña, and K. Landsteiner, *Front. in Phys.* **12**, 1460268 (2024), [arXiv:2407.04372 \[hep-th\]](#) .
- [58] B. Cownden, C. Pantelidou, and M. Zilhão, *JHEP* **05**, 202 (2024), [arXiv:2312.08352 \[gr-qc\]](#) .
- [59] V. Boyanov, V. Cardoso, K. Destounis, J. L. Jaramillo, and R. Panosso Macedo, *Phys. Rev. D* **109**, 064068 (2024), [arXiv:2312.11998 \[gr-qc\]](#) .
- [60] D. Garcia-Fariña, K. Landsteiner, P. G. Romeu, and P. Saura-Bastida, (2024), [arXiv:2407.06104 \[hep-th\]](#) .
- [61] D. Areán, D. G. Fariña, and K. Landsteiner, *JHEP* **12**, 187 (2023), [arXiv:2307.08751 \[hep-th\]](#) .
- [62] V. Boyanov, K. Destounis, R. Panosso Macedo, V. Cardoso, and J. L. Jaramillo, *Phys. Rev. D* **107**, 064012 (2023), [arXiv:2209.12950 \[gr-qc\]](#) .
- [63] Y. Yang, Z.-F. Mai, R.-Q. Yang, L. Shao, and E. Berti, *Phys. Rev. D* **110**, 084018 (2024), [arXiv:2407.20131 \[gr-qc\]](#) .
- [64] E. Berti, V. Cardoso, M. H.-Y. Cheung, F. Di Filippo, F. Duque, P. Martens, and S. Mukohyama, *Phys. Rev. D* **106**, 084011 (2022), [arXiv:2205.08547 \[gr-qc\]](#) .
- [65] K. Kyutoku, H. Motohashi, and T. Tanaka, *Phys. Rev. D* **107**, 044012 (2023), [arXiv:2206.00671 \[gr-qc\]](#) .
- [66] T. Torres, *Phys. Rev. Lett.* **131**, 111401 (2023), [arXiv:2304.10252 \[gr-qc\]](#) .
- [67] R. F. Rosato, K. Destounis, and P. Pani, *Phys. Rev. D* **110**, L121501 (2024), [arXiv:2406.01692 \[gr-qc\]](#) .
- [68] N. Oshita, K. Takahashi, and S. Mukohyama, *Phys. Rev. D* **110**, 084070 (2024), [arXiv:2406.04525 \[gr-qc\]](#) .
- [69] L.-M. Cao and L.-B. Wu, *Phys. Rev. D* **103**, 064054 (2021), [arXiv:2101.02461 \[gr-qc\]](#) .
- [70] E. Abdalla, R. A. Konoplya, and C. Molina, *Phys. Rev. D* **72**, 084006 (2005), [arXiv:hep-th/0507100](#) .
- [71] R. A. Konoplya and A. Zhidenko, *Phys. Rev. D* **77**, 104004 (2008), [arXiv:0802.0267 \[hep-th\]](#) .
- [72] R. A. Konoplya and A. Zhidenko, *Phys. Rev. D* **82**, 084003 (2010), [arXiv:1004.3772 \[hep-th\]](#) .
- [73] G. Dotti and R. J. Gleiser, *Class. Quant. Grav.* **22**, L1 (2005), [arXiv:gr-qc/0409005](#) .
- [74] D. Yoshida and J. Soda, *Phys. Rev. D* **93**, 044024 (2016), [arXiv:1512.05865 \[gr-qc\]](#) .
- [75] G. Dotti and R. J. Gleiser, *Phys. Rev. D* **72**, 044018 (2005), [arXiv:gr-qc/0503117](#) .
- [76] R. J. Gleiser and G. Dotti, *Phys. Rev. D* **72**, 124002 (2005), [arXiv:gr-qc/0510069](#) .
- [77] J. P. Boyd, *Chebyshev and Fourier spectral methods* (Courier Corporation, 2001).
- [78] J.-N. Chen, L.-B. Wu, and Z.-K. Guo, *Class. Quant. Grav.* **41**, 235015 (2024), [arXiv:2407.03907 \[gr-qc\]](#) .
- [79] J. P. Boyd, *Journal of Computational Physics* **126**, 11 (1996).
- [80] C. M. Markakis, M. F. O'Boyle, D. Glennon, K. Tran, P. Brubeck, R. Haas, H.-Y. Schive, and K. Uryū, (2019), [arXiv:1901.09967 \[math.NA\]](#) .
- [81] C. Markakis, S. Bray, and A. Zenginoğlu, (2023), [arXiv:2303.08153 \[gr-qc\]](#) .
- [82] L. J. G. Da Silva, (2024), [arXiv:2401.08758 \[gr-qc\]](#) .
- [83] M. F. O'Boyle, *Time-symmetric integration of partial differential equations with applications to black hole physics*, Ph.D. thesis, Illinois U., Urbana (main) (2022).
- [84] E. S. C. Ching, P. T. Leung, W. M. Suen, and K. Young, *Phys. Rev. Lett.* **74**, 2414 (1995), [arXiv:gr-qc/9410044](#) .
- [85] E. S. C. Ching, P. T. Leung, W. M. Suen, and K. Young, *Phys. Rev. D* **52**, 2118 (1995), [arXiv:gr-qc/9507035](#) .
- [86] M. F. O'Boyle, C. Markakis, L. J. G. Da Silva, R. Panosso Macedo, and J. A. V. Kroon, (2022), [arXiv:2210.02550 \[gr-qc\]](#) .
- [87] L. J. G. Da Silva, R. Panosso Macedo, J. E. Thompson, J. A. V. Kroon, L. Durkan, and O. Long, (2023), [arXiv:2306.13153 \[gr-qc\]](#) .
- [88] V. Cardoso, S. Yoshida, O. J. C. Dias, and J. P. S. Lemos, *Phys. Rev. D* **68**, 061503 (2003), [arXiv:hep-th/0307122](#) .
- [89] Y. Ashida, Z. Gong, and M. Ueda, *Adv. Phys.* **69**, 249 (2021), [arXiv:2006.01837 \[cond-mat.mes-hall\]](#) .
- [90] E. Gasperin and J. L. Jaramillo, *Class. Quant. Grav.* **39**, 115010 (2022), [arXiv:2107.12865 \[gr-qc\]](#) .
- [91] J. Besson and J. L. Jaramillo, (2024), [arXiv:2412.02793 \[gr-qc\]](#) .
- [92] T. F. M. Spieksma, V. Cardoso, G. Carullo, M. Della Rocca, and F. Duque, (2024), [arXiv:2409.05950 \[gr-qc\]](#) .
- [93] M. H.-Y. Cheung, K. Destounis, R. P. Macedo, E. Berti, and V. Cardoso, *Phys. Rev. Lett.* **128**, 111103 (2022), [arXiv:2111.05415 \[gr-qc\]](#) .
- [94] V. Boyanov (2024) [arXiv:2410.11547 \[gr-qc\]](#) .